A ternary Neurexin-T178-PTPR complex represents a core-module of neuronal synapse organization

by

Spyros Thivaios[1*], Jochen Schwenk[1* #], Aline Brechet[1], Sami Boudkkazi[1], Phil Henneken[1], Maciej K. Kocylowski[1], Alexander Haupt[1], Debora Kaminski[2,3], Jean-Baptiste van den Broucke[1], Dietmar Schreiner[4], Uwe Schulte[1,5], Fredrik H. Sterky[2,3,6], Michisuke Yuzaki[7], Peter Scheiffele[4], Bernd Fakler[1,8,9 #]

[1] Institute of Physiology, Faculty of Medicine, University of Freiburg, Hermann-Herder-Str. 7, 79104 Freiburg, Germany

[2] Department of Laboratory Medicine, Institute for Biomedicine, Sahlgrenska Academy, University of Gothenburg, Gothenburg, Sweden

[3] Department of Clinical Chemistry, Sahlgrenska University Hospital, Gothenburg, Sweden

[4] Biozentrum of the University of Basel, 4056 Basel, Switzerland

[5] Logopharm GmbH, Schlossstr. 14, 79232 March-Buchheim, Germany

[6] Wallenberg Centre for Molecular and Translational Medicine, University of Gothenburg, Gothenburg, Sweden

[7] Department of Neurophysiology, Keio University School of Medicine, Tokyo, Japan

[8] Signalling Research Centres BIOSS and CIBSS, Schänzlestr. 18, 79104 Freiburg, Germany

[9] Center for Basics in NeuroModulation, Breisacherstr. 4, 79106 Freiburg, Germany

* authors with equal contribution

[#]To whom correspondence should be addressed

Email: jochen.schwenk@physiologie.uni-freiburg.de (J.S.) or
bernd.fakler@physiologie.uni-freiburg.de (B.F.)

Summary

Complexes of synaptic adhesion molecules instruct the formation, functional specification and plasticity of neuronal synapses. Proteomic and candidate gene studies have identified an array of synaptic adhesion molecules that may cooperate or provide independent columns connecting synaptic compartments, thereby, promoting the nucleation of presynaptic active zones and recruitment of postsynaptic neurotransmitter receptors.
Here, we used a systematic large-scale multi-epitope affinity-purification approach (total of >120 purifications with 30 target proteins), combined with quantitative mass spectrometry to comprehensively map trans-synaptic protein networks in the mouse brain. We discover a universal presynaptic core-module consisting of the neurexin proteins and LAR-type receptor protein tyrosine phosphatases (PTPRD,S,F), linked by the tetraspanin proteins T178A, B. These ternary Neurexin-T178-PTPR complexes form through their trans-membrane domains and assemble during biogenesis in the ER. Loss of T178B results in module dissociation and loss of LAR-PTPRs. At synapses, the Neurexin-T178-PTPR module recruits stable trans-synaptic protein networks with specific pre- and post-synaptic partners and secreted extracellular linkers. These networks encompass stable associations with unique postsynaptic GABAergic and glutamatergic neurotransmitter receptor complexes, identifying the Neurexin-T178-PTPR module as a central, universal integrator of trans-synaptic signaling in the central nervous system.

Introduction

Synapses are sophisticated communication units that facilitate the transmission of information between cells in the central nervous system. The structural and functional diversity of synapses is astonishing and fundamental for nervous system operation. Cell adhesion systems drive a substantial degree of the formation and stabilization of neuronal synapses. Amongst multiple structurally and functionally distinct adhesion molecules, neurexins (NRXs) stand out as one class of synaptic organizers which nucleate protein assemblies that instruct formation and functional properties of synapses (Gomez et al., 2021; Sudhof, 2017). Thus, NRXs direct presynaptic active zone assembly, impact Ca^{2+}-dependent neurotransmitter release, and instruct trans-synaptic nano-alignments and function of post-synaptic receptors in mice, flies and worms (Aoto et al., 2015; Chen et al., 2017; Dean et al., 2003; Graf et al., 2004; Kurshan et al., 2018; Matsuda and Yuzaki, 2011; Missler et al., 2003; Nozawa et al., 2022; Owald et al., 2012; Uemura et al., 2010).

The majority of NRX proteins are presynaptic single-pass transmembrane proteins. In mammals, NRXs are expressed from three genes with alternative promotor usage generating long (α-neurexin) and short (β-neurexin) isoforms

(Hauser et al., 2022; Schreiner et al., 2014; Sudhof, 2017; Ushkaryov et al., 1992); in addition, for *Nrxn1*, a very short γ-neurexin isoform is expressed from a third alternative promoter (Sterky et al., 2017; Yan et al., 2015) (Figure 1A). What makes NRXs unique amongst other synaptic adhesion molecules is their extensive molecular diversification through alternative splicing. Inclusion of alternative exons at six spliced segments (AS1-AS6) generates high numbers of variants with differential expression in neuronal cell types (Furlanis et al., 2019; Nguyen et al., 2016; Schreiner et al., 2014; Treutlein et al., 2014; Ullrich et al., 1995). This molecular complexity together with splice isoform-specific binding to interaction partners instructs the specificity of synaptic cell-cell communication. Widely studied interactors include neuroligins (NLGNs), leucine-rich repeat transmembrane neuronal proteins (LRRTMs) and cerebellins (CBLNs), all proteins which themselves regulate synapse formation and/or maturation (Aoto et al., 2013; Bhouri et al., 2018; Chih et al., 2006; de Wit et al., 2009; Ito-Ishida et al., 2012; Ko et al., 2009; Seigneur and Sudhof, 2017; Uemura et al., 2010; Um et al., 2016).

From recent studies it emerged that synapse formation in the CNS is unlikely to be driven by a single molecular synapse-organizing system, but rather results from multiple independent modules that operate synergistically either in parallel or together, connected via intracellular scaffolds and/or extracellular linkers. Besides the NRXs, presynaptic leukocyte common antigen-related receptor protein tyrosine phosphatases (LAR-PTPRs: PTPRD, S and F) are thought to operate as second major hub(s) for synapse organization (Li et al., 2015; Ozel et al., 2019; Park et al., 2020; Roppongi et al., 2020; Takahashi and Craig, 2013). These PTPRs are largely co-expressed with NRXs and interact with several common post-synaptic partners thus indicating that both, LAR-PTPR and NRX modules, may co-operate in synapse development (Han et al., 2020; Roppongi et al., 2020). Moreover, recent knockout studies suggested redundancy of LAR-PTPRs and NRX functions, as only their combined deletion severely impaired synapse development in cerebellar circuits (Sclip and Sudhof, 2023). Importantly, LAR-PTPRs exhibit evolutionarily conserved cytoplasmic interactions with key regulators of active zone assembly, most prominently complexes of SYD-1 and SYD-2/Liprin-α (LIPA) proteins (Dai et al., 2006; Marco de la Cruz et al., 2024; Muhammad et al., 2015; Owald et al., 2012; Wentzel et al., 2013; Wong et al., 2018).

Understanding the organizing principles and relation of multiple cell adhesion systems expressed in *cis* in the same synaptic membrane, such as NRXs and LAR-PTPRs, remains a major unresolved question. Its pursuit requires comprehensive and quantitative analysis of native protein complexes in synaptic membranes of the brain as is enabled by proteomic technologies combining multi-epitope affinity-purifications (meAPs) with quantitative high-resolution mass spectrometry (nano-LC MS/MS).

Here we built on a proteomic workflow that has been successfully applied to decipher subunit assembly and protein-protein interactions of various types of integral membrane proteins (Kocylowski et al., 2022; Kollewe et al., 2021; Kollewe et al., 2022; Muller et al., 2010; Schmidt et al., 2017; Schwenk et al., 2012; Schwenk

et al., 2010; Schwenk et al., 2016). We refined this approach for systematic analysis of trans-synaptic adhesion complexes by applying meAPs targeting all three NRX isoforms and reciprocal 'reverse meAPs' for major NRX interaction partners. Surprisingly, we find that the majority of NRXs in the adult mouse brain co-assembles with LAR-PTPRs and proteins T178A/B, a family of yet uncharacterized tetraspanins, into stable ternary complexes. Detailed sets of reverse meAPs uncovered these ternary complexes as 'core-modules' of extended protein networks that organize presynaptic signaling entities and establish stable associations with several major classes of post-synaptic effectors including neurotransmitter-receptor complexes and synaptic organizers. Thus, *cis*-interactions with NRXs generate a presynaptic organization platform that integrates synaptic interactions through multiple trans-synaptic interaction modules.

Added Note:
Proteins will be referred to by the acronyms used in the UniProt/SwissProt database throughout, descriptive names or gene names may be taken from Table 1 or text.

Results

Native neurexins are embedded into extended synaptic protein networks

Interactions of recombinant NRX proteins have been extensively studied *in vitro*. However, their molecular appearance and interactomes in native tissue remain largely unknown. To obtain a detailed map of native NRX complexes in the mouse brain, we developed a comprehensive high-resolution proteomics approach combining multi-epitope affinity-purifications with quantitative mass spectrometry (meAP-MS; Methods). This approach leverages a set of 15 validated antibodies (ABs) targeting the primary NRX isoforms via epitopes that are either isoform-specific (anti-NRX1, anti-NRX2, anti-NRX3) or present in all NRXs (anti-NRX1-3 or pan-NRX) and that are located at various positions along the primary sequences (Figure 1A, left, Methods). The input for the meAPs were detergent (CL-91)-solubilized membrane-fractions prepared from adult mouse brains (Methods) which contained all three primary NRX isoforms. In fact, quantitative MS detected NRX1-3 in these plasma membrane-enriched fractions at distinct amounts with NRX1 and NRX3 paralogues being the most abundant (Figure 1B). Surprisingly, we found similar amounts for both the canonical long NRX1α and the only recently recognized short γ-isoform of NRX1, highlighting NRX1γ as a major NRX1 proteoform in the mouse brain (Figure 1B, *Figure S1*).

To uncover native NRX protein complexes, the four independent anti-NRX1-3 ABs were used in a first round of APs as target-specific ABs, together with pools of pre-immunization IgGs and pre-immunization sera as negative controls. All resulting AP-elutions were analyzed by high-resolution nano-LC MS/MS and evaluated by label-free quantification based on peak-volumes (PVs). This procedure offers a linear dynamic range of more than four orders of magnitude for quantification of protein amounts (Bildl et al., 2012; Boudkkazi et al., 2023; Schulte et al., 2023). The respective results showed effective purification of the NRX isoforms indicated by large PVs and broad/extensive coverage of the primary sequences by MS/MS-identified peptides (*Figure S2*). In addition to the NRX targets, the APs retrieved large numbers of additional proteins (exceeding the detection threshold of our MS analyses, Methods) that were evaluated for their target-specific co-purification, as well as for consistency and direct comparability across the individual APs. The latter was done by determining for any protein target-normalized ratios (tnRs, (Kocylowski et al., 2022)) which is the relative abundance of a protein related to both, AP-background (minimal value derived from negative controls) and AP-target (maximal value; Methods, *Figure S3*). When analyzed by t-SNE (t-distributed stochastic neighbor embedding), the resulting plot of the tnR-values obtained in APs with the four anti-NRX1-3 ABs (*Figure S3*, Table 1) immediately identified a perfectly separated cluster of (roughly 45) proteins that tightly co-localized around the targets, thus indicating robust and consistent co-purification with the anti-NRX1-3 ABs in all APs (Figure 1C, *Table S1*). Closer inspection uncovered notable features of these target-clustered proteins (Figure 1C, inset, Table 1): (1) They are components of the pre- and post-synaptic compartment, and the synaptic cleft, (2) most identified

proteins are either single-pass trans-membrane or soluble/secreted proteins, and (3) several of them were established interaction partners of the NRX proteins, such as neurexophilins (NXPH1-4, (Missler and Sudhof, 1998)), cerebellins (CBLN1-3, (Matsuda and Yuzaki, 2011)), carbonic anhydrase-related (CAH) proteins 10, 11 (Sterky et al., 2017), chemokine-like proteins TAFA1,2 (Khalaj et al., 2020), amyloid-β precursor protein (A4 or APP, (Cvetkovska et al., 2022)), receptor protein tyrosine phosphatase S (PTPRS, (Roppongi et al., 2020)) or leucine-rich repeat transmembrane neuronal (LRRT) proteins 1-4 (de Wit et al., 2009; Siddiqui et al., 2010). In addition, the cluster contained a substantial number of proteins that were previously unknown to be associated with NRXs. These proteins include the tetraspanins T178A and T178B, the putative lipid scramblase XK-related protein 6 (XKR6), reticulon-4 receptor (RTN4R, also termed NoGo receptor) and reticulon-4 receptor like 1 (R4RL1), as well as amyloid-β precursor-like protein (APLP2), ITM2B, C (Schwenk et al., 2016), and the LAR-type receptor protein tyrosine phosphatases PTPRD and F. Interestingly, quantitative analysis of protein abundances in source material ('expression in membrane fractions') and AP-elutions showed that the two PTPRs D and S, and the tetraspanin protein T178B were co-purified in almost complete amounts and in close to stoichiometric ratio(s) with the NRXs (Figure 1D), in line with co-expression of PTPRs, NRXs and T178s in the entire brain (*Figure S4*).

In a next round of APs, we used isoform-specific ABs and target-knockouts (*Figure S5*) as stringent negative controls to uncover whether these novel interactors associate selectively with any of the NRX isoforms or whether they co-assemble with all primary NRX proteins. Importantly, we discovered that NRX1, 2, and 3 do not mutually co-purify (Figure 1E) indicating that they form separate molecular entities. While some of the aforementioned interactors, like CAH11, R4RL1 and LRRTM2, exhibited preferences for individual NRXs, others co-assembled with all three NRX isoforms (Figure 1E, *Table S1*). Most prominently, PTPRs and T178B were highly abundant in all NRX APs. Moreover, XKR6 was also commonly recovered with all NRXs in the APs, albeit at markedly lower amounts (Figure 1D). Together, these meAP-MS data demonstrated that in the adult brain the three NRX paralogues form separate trans-synaptic modules with numerous interactors. However, all three NRXs co-assemble with T178B and LAR-PTPRs into previously unrecognized stoichiometric complexes.

Neurexins form ternary core-modules with T178 and LAR-type PTPRs

The co-assembly of NRXs with T178 and LAR PTPRs was further investigated by native gel electrophoresis and reverse APs. Native gel separation of brain membrane fractions indicated tight co-migration of NRX1, LAR-PTPRs and T178B at an apparent molecular mass of roughly 400 kDa (Figure 2A, arrowhead). This value suggested an equimolar (or 1:1:1) stoichiometry for the constituents of the ternary NRX-T178-LAR-PTPRs complexe(s) based on predicted protein mass (Table 1). In addition, the native gels demonstrated assembly of the ternary complex with multiple additional partners/interactors as reflected by the extension of all three

Western blot signals into the higher apparent mass range (Figure 2A). Orthogonal ('reverse') APs with ABs against both, PTPRS and T178B, robustly retrieved the NRX proteins together with multiple of their interaction partners as shown by the respective tnR-values (Figure 2B). Accordingly, the ternary NRX-T178-LAR-PTPRs complex may be considered a 'core-module' of larger assemblies whose constituents were consistently and robustly co-purified in the meAP experiments (Figure 1C, E, Figure 2B, Table 1).

Next, we investigated the structural determinant(s) for the assembly of the ternary core-module in native tissue by comparative APs (Figure 2C, D, insets) dissecting the role of the extracellular domain versus the transmembrane and intracellular stretches, and the significance of the heparan sulfate moieties (Zhang et al., 2018). We targeted the endogenous GPI-anchored NRX3 AS5 splice variant tagged through the knock-in of an HA-epitope (NRX3 AS5$^{(HA/HA)}$, (Hauser et al., 2022)) and compared the recovery of the core module components to APs for total NRX3 (Figure 2C). MS-based quantification indicated that assembly into the core-module is abolished for the splice-variant lacking the transmembrane domain, while binding of the soluble interactors (CBLNs or TAFAs) to the extracellular domains of NRX3 was largely preserved in the NRX3 AS5 proteoform (Figure 2C). In contrast, removal of heparan sulfation markedly decreased co-purification of post-synaptic interactors (including LRRTs and AMPA-type glutamate receptors (AMPARs)), but neither affected assembly of the core-module nor its association with soluble partner proteins (Figure 2D). Moreover, assembly of the core-module did not require any additional components as indicated by the robust complex formation observed upon heterologous reconstitution/expression of all three constituents (Figure 2E, *Figure S6*). Interestingly, effective co-purification of PTPRS and NRX1A or NRX3A strongly depended on the presence of T178 in these AP-experiments, while weak interaction between the NRX and PTPR was observed upon their pairwise expression in the absence of the tetraspanin (Figure 2E). Likewise, binding of GPI-anchored NRX3A to PTPRS was weak and independent of T178B (*Figure S6A*). Thus, the transmembrane domain of NRX and the short cytoplasmic domain are obligatory for formation of the ternary core-module, while the extended extracellular portion of the NRX protein is not able to promote core-module assembly.

We complemented these biochemical experiments with 'molecular docking' studies performed with AlphaFold2. The results predicted a 3D-structural arrangement (Methods) for the membrane-proximal regions of the ternary core-module where the transmembrane domains of NRX and PTPR are juxtaposed and surrounded by three of the four transmembrane segments of T178B (Figure 2F, left panel; *Figure S6B*). In this framework, T178B is expected to closely link the two major classes of cell adhesion molecules, and to generate a macro-molecular complex with an extended surface for protein-protein interactions both in the membrane plane, as well in the aqueous phases on either side of the membrane (Figure 2F, right panel).

Assembly of the core-module(s) in the ER and significance of T178B knock-down

The structural arrangement of the ternary core-module and the association of its constituents with multiple partner proteins prompted the questions on where co-assembly of NRX, T178 and LAR-PTPRs occurs and what may happen upon targeted removal of the interlinking T178B protein. For this purpose, we first investigated the molecular appearance of the core-module constituents in a protein fraction highly enriched for ER-membranes (Schwenk et al., 2019) by complexome-profiling via csBN-MS, a technique that combines native gel electrophoresis with quantitative mass spectrometry (Figure 3A, inset, (Kollewe et al., 2021; Muller et al., 2019; Schulte et al., 2023).

The 'abundance-mass profiles' obtained with this technique demonstrated effective co-assembly of NRX1A, T178B and PTPRS, D in the ER, most prominently reflected by the profile-peaks at an apparent mass of around 400 kDa (Figure 3A, shaded), identical to the result obtained with the plasma membrane-enriched fractions before (Figure 2A). The abundance-peak of T178A at a slightly smaller mass (~360 kDa) together with the broadening ('shoulder') of the peaks in the LAR-PTPRs and NRX1A profiles argues for preferred co-assembly of this tetraspanin with variants of the PTPRs and NRXs. Interestingly, the ER-profiles also showed formation of higher-mass assemblies (up to 1.2 MDa) indicating association of the core-module with further interactors. We explored the subunits of these assemblies by additional APs with anti-NRX1-3 and anti-PTPRS ABs and identified association with liprin-α2 (LIPA2), Cav2.2 (CAC1B), CAH10 and CBLN1 amongst other proteins (*Table S2*). Thus, our csBN-MS data identified formation of the core-module during biogenesis in the ER and suggested its delivery to the plasma membrane as a pre-formed entity together with co-assembled partners.

Next, we explored the consequences of targeted knockdown of the NRX-PTPR-linking T178B protein by virally-driven expression of two different shRNAs (sh-T178B-1, -2) in both neuronal cultures and hippocampal neurons in living mice. In cultured neurons, AAV-delivered sh-T178B decreased the amount of the T178B protein present in (un-solubilized) membrane fractions by more than 95% as determined by quantitative MS (Figure 3B, *Table S3*). More detailed analysis showed that this decrease was target-selective/specific leaving the vast majority of proteins in this fraction either unaltered or changed by less than 10% (Figure 3B, red lines). In contrast, MS-quantification detected distinct alterations in the abundance of the core-module constituents: While PTPRS,D and NRX3 were decreased by 40% and 20%, respectively, NRX2 (together with some NRX-interactors) was increased by about 20%. These changes in 'expressed protein amounts' translated into profound alterations in the composition of the core-module and its assemblies uncovered by anti-PTPRS and anti-NRX1-3 APs (Figure 3C, *Table S3*). Thus, (1) the ternary complexes were largely abolished, leaving NRX and PTPRs either as separate proteins, or, as a minor portion of bi-molecular NRX-PTPR assemblies, (2) NRX, despite unchanged purification efficiency (compared to WT), lost 30-60% of its postsynaptic interactors such as LRRTs or NLGNs, as well

as PTPR-linked presynaptic partners such as liprins (LIPA3) or proteins LRFN (leucine-rich repeat and fibronectin type-III domain containing), and (3) PTPRS was largely deprived of its NRX-recruited interactors including the CBLNs (Figure 3C). In addition, the increased co-purification of SYT11, a vesicular protein involved in protein processing/trafficking (Trovo et al., 2024), argued for an increased pool of PTPRs and NRXs residing in intracellular membrane compartments. This was confirmed by anti-PTPRS stainings of hippocampal neuronal cultures upon knockdown of T178B (Figure 3D).

The significance of the knockdown-induced changes was further pursued in the hippocampus of adult mice where the AAV-sh-T178B was delivered into the hippocampus (CA3 region, *Figure S7)* of one hemisphere by stereotactic injection, while the other was left untouched for the use as wildtype control (WT, Methods). As illustrated in Figure 3E, whole-cell recordings performed in acute slices detected AMPAR-mediated excitatory post-synaptic currents (EPSCs) in response to spontaneous action potentials in pyramidal neurons of the CA1 region (CA1 PCs) in both hemispheres. These sEPSCs were slightly increased in amplitude in the injected hemisphere, but appeared largely unaltered in their time course (Figure 3E, upper panel). In contrast, EPSCs evoked by electrical stimulation of the Schaffer collaterals (Figure 3E, inset), the axons of CA3 PCs serving as presynaptic input to the CA1 PCs, uncovered marked differences between non-injected and virus-injected hemispheres. While control CA1 PCs responded with constant EPSCs in paired-pulse (PP) recordings (PP-ratio ~100%) at stimulation frequencies of 10 and 50 Hz, PCs in the injected hemispheres displayed a marked stimulation-dependent increase in their EPSC amplitudes (PP-ratios of 150-200%; Figure 3E, lower panel). This increase in PP-ratio was induced by the knock-down of T178B in the pre-synaptic terminals, but independent from knock-down in the post-synaptic neuron, pointing towards altered presynaptic function(s) in the absence of T178B (Figure 3E, lower panel, *Figure S7*).

Together, these results on selective removal/reduction of T178B indicated the importance of this protein for formation of the ternary NRX-T178-PTPR complexes and demonstrated the significance of their structural integrity for normal synaptic transmission. Notwithstanding, they also showed that the remaining entities enabled operation of pre-synapses, albeit with characteristics that were different from normal presumably as a consequence of altered protein arrangements/assemblies.

Integration of the Neurexin-T178-PTPR module into pre- and trans-synaptic protein networks

To test whether the NRX-T178-PTPR core selectively engages in specific trans-synaptic interactions or whether it represents a universal synapse-building block, we performed a series of reverse meAP-MS-experiments targeting an array of NRX-interactome constituents (Figure 1, Table 1). In total, 30 different constituents were selected as targets prioritized to cover (1) all three synaptic compartments, pre- and post-synaptic membrane, or the synaptic cleft and to cover (2) the diverse physiological functions annotated in literature and public databases (Figure 5, upper

panel, Table 1). Experimentally, all reverse 64 target meAPs (plus 27 control APs) were performed and rigorously evaluated as described before; in particular, specificity of co-purification (in APs with 1-4 ABs per target) was determined from MS-based tnR-values with target-KOs and/or pre-immunization IgGs as negative controls and an empirically-determined tnR-value of 0.25 as a specificity threshold (Kocylowski et al., 2022; Kollewe et al., 2022). The complete sets of proteins determined as specific interaction partners of a given target, together with all details related to the respective meAP experiments are summarized in *Table S4*.

Figure 4 illustrates the t-SNE plots of tnR-values obtained in multiple APs with six of the 30 selected targets (Figure 4, central inset): in the pre-synapse (PTPRS and CAH10, a protein covalently bound to NRX1-3 (Sterky et al., 2017)), in the synaptic cleft (CBLN1/2, neurexophilin 3 (NXPH3) and TAFA1) and in the post-synaptic membrane (LRRT4). Similar to the anti-NRX1-3 APs (Figure 1C), these t-SNE plots of reverse APs readily delineated well-defined clusters of proteins identified as specific and consistent target-interactors by their tight co-localization with the respective target (Figure 4, insets, blue frame(s)). This finding immediately indicated that all the NRX-associated target proteins were affinity-isolated as constituents of larger assemblies built on robust detergent-resistant protein-protein interactions. Remarkably, all these assemblies contained the molecularly diverse constituents of the NRX-T178-PTPR core-module (Figure 4) highlighting their common incorporation into the examined synaptic protein complexes. Beyond the ternary core-module, the t-SNE-delineated assemblies contained two groups of additional constituents. One group of proteins was shared among several of the isolated assemblies and thus likely forms an integral part of the central NRX-based building block(s), such as CBLNs, CAH10/11, or XKR6. The other group was uniquely detected with individual targets thus indicating their co-assembly with the NRX-based building block(s) in a target-dependent manner. These selectively associated proteins represented a variety of distinct functional classes including proteins involved in cell adhesion, neuronal/axonal growth and development, voltage- and ligand-gated ion channels, G-protein coupled receptors (GPCRs), lipid-modulation, vesicle-fusion/processing or extracellular matrix (ECM).

As an additional finding of major importance, the t-SNE plots showed that pre-synaptic targets (PTPRS and CAH10-NRXs) robustly co-purified integral post-synaptic membrane proteins (including LRRT1,3,4, and the AMPAR-subunits GRIA1-3, GSG1l, SHSA7, and NOE1 (Schwenk et al., 2012)), and vice versa. Accordingly, the NRX-T178-PTPR core-modules establish proteinaceous trans-synaptic bridges that are stable enough for effective quantitative affinity-isolation and that firmly link pre- and post-synaptic membrane proteins (Figure 4).

Together, these reverse meAPs strongly suggested that the NRX-T178-PTPR module(s) are central hub elements of extended protein networks that expand within and across the synaptic membranes and that are built from a conserved core and a molecularly variable periphery.

The synaptic connectome of the Neurexin-T178-PTPR core module

For insight into the structure and complexity of these networks, we next explored their strings and (sub)-clusters by detailed analyses of the core module-associated interactomes (Table 1, *Table S4*) for protein-protein interactions documented by specific co-purification(s) and formed between individual or groups of constituents. Moreover, we used the quantitative data on protein abundances for automated cluster-analysis with the UMAP-algorithm (McInnes et al., 2018) (Methods, *Figure S8*). Finally, we projected the results of these analyses combined with established sub-cellular localization(s) of individual protein constituents onto the synaptic topology.

Figure 5 depicts the derived multi-protein network. Robust interactions between the constituents are represented by lines that each indicate effective co-purification in APs using the respective constituent(s) as an AP-target (encircled in red). Note, that the illustration does not contain all specific interactors identified in the meAPs (*Table S4*); the complete set, however, is accessible through an interactive figure version made available online (URL).

The NRX-T178-PTPR module in its molecularly diverse composition forms the central core/hub element that recruits interactors with distinct structural and functional properties in all three compartments of the synapse (Figure 5, *Figure S8*). In the pre-synapse, consistent with a role in differentiation of axonal terminals, the NRX-T178-PTPR module co-assembles with key effectors of the active zone (UN13A, LIPA2/3, voltage-gated Ca^{2+} channels of the Cav2-family, and BK_{Ca}-type K^+ channels (KCMA1)), as well as with pre-synaptic signaling receptors such as the metabotropic glutamate receptor GRM4, and the metabotropic glycine receptor (MGLYR/GPR158)-RGS7 complex (Laboute et al., 2023). Remarkably, we further identified close associations of the NRX-T178-PTPR core-module with several surface receptors previously implicated in neuronal development (and axonal pathfinding) such as RTN4R, R4RL1, ASTN1, NEGR1, the A4/APP-APLP2-ITM2B complex (Schwenk et al., 2016) or T132A, a suspected regulator of integrins and integrin pathway (Li et al., 2022). This suggests that the core-module serves as an organizing platform for the lateral recruitment of adhesive (signaling) elements in addition to the established NRX- and PTPR-based adhesions. Finally, XKRs 4 and 6 were discovered as tight interactors of the core-module. XKR4 is a bonafide lipid scramblase, raising the possibility for local lipid signaling at NRX-based synaptic terminals (Neniskyte et al., 2023). Together, the NRX-T178-PTPR module and its partner proteins reconstitute a multi-component platform for spatial organization of presynaptic functions.

The cleft-located portion of the network consists of secreted proteins attached to the core-module either via covalent bonding (CAH10, TAFA1) or direct protein-protein interactions (NXPHs, CBLNs, C1QL3, or NOE1 (Boudkkazi et al., 2023)). These constituents exhibit a two-tiered characteristic: First, they stabilize the presynaptic platform by providing additional connectivities between the core-module and several of its presynaptic partners (XKR6, GRM4 or KCMA1). Second, they establish tight linkages between the core-module and integral components of the

post-synaptic membrane. Most prominently these links directly target the neurotransmitter receptors for excitatory (AMPARs and kainate-receptors (GRIK2)) and inhibitory synaptic transmission (glycine receptors (GLRA1)).

Beyond the cleft-mediated trans-synaptic linkages, the NRX-T178-PTPR-associated network establishes direct connections to several post-synaptic membrane proteins, including AMPARs and $GABA_A$-receptors ($GABA_ARs$), as well as LRRTs, and the cell-adhesion proteins LRFN1/3 and LRC4B. Interestingly, AMPAR and $GABA_AR$ complexes (*Table S4*) display very different network integration: While AMPARs are linked to the core-module through several different strings (NOE1-NRX-CAH10, GSG1l-LRRT4), $GABA_ARs$ predominantly rely on the NRX-NLGN binding (Figure 5). Importantly though, the network structure provides immediate interconnection(s) between the post-synaptic neurotransmitter receptor-complexes and the pre-synaptic active-zone thus juxtaposing sites for transmitter release and transmitter-gated effector channels introduced as 'nano-column' organization before (Biederer et al., 2017; Tang et al., 2016).

The synaptic multi-protein network shown in Figure 5 represents the comprehensive connectome of the NRX-T178-PTPR module determined in membrane fractions of the entire adult mouse brain. Accordingly, the annotated constituents are not expected to be present in every synaptic network. Rather individual synapses will use selected sets of this network (*Figure S8*) depending on the type of neuronal communication or the stage of development and differentiation. Notwithstanding, the NRX-T178-PTPR connectome provides the molecular framework for the complex NRX-functions in brain synapses by (1) emphasizing the robustness of the trans-synaptic network, (2) identification of its constituents, including a considerable number of proteins not previously related to NRX-biology or with not yet resolved primary function(s), and (3) definition of their pair- and group-wise connectivities by detergent-resistant protein-protein interactions.

Discussion

This work aiming at comprehensive analysis of the NRX family of cell adhesion molecules in the rodent brain uncovered intimate assembly of the NRXs with LAR-type PTPRs and the tetraspanins T178A, B into stable ternary complexes. In synapses, these complexes act as core-modules of extended trans-synaptic protein networks that recruit various classes of signaling entities into close spatial proximity in the pre-synapse and form solid associations with neurotransmitter and other receptors in the post-synapse. Accordingly, the NRX-T178-PTPR modules may be considered as central universal integrators of trans-synaptic signaling in the mammalian brain.

Molecular appearance of native NRXs and associated networks - technical aspects of the proteomic analyses

For thorough and unbiased analysis of the molecular appearance of native NRXs as present in the adult rodent brain, we applied a largely refined proteomic workflow of meAP-MS that promotes comprehensiveness and specificity of the pursued interactomes (and interaction partners) by means of its key features (Kocylowski et al., 2022; Kollewe et al., 2022; Schmidt et al., 2017; Schwenk et al., 2012; Schwenk et al., 2016): (1) use of solubilization conditions that preserve native higher molecular mass complexes of the target (based on careful buffer assessment via BN-PAGE and MS-analysis), (2) application of multiple verified ABs with distinct epitopes on each target (Figure 1, *Table S4*), (3) MS-based protein quantification with a linear range of about four orders of magnitude and unbiased identification of all proteins, (4) the use of stringent negative controls (knockout input, target-unrelated ABs) and (5) consistency among ABs for determination of interactome constituents (visualized by t-SNE plots of tnR-values). With respect to criteria (4) and (5), it must be noted that our meAP-MS approach aims at high reliability and a minimal number of false-positive interactors, deliberately operating at the cost of false negatives.

As an immediate outcome, this approach identified stoichiometric co-assembly of NRXs1-3 with all three LAR-type PTPRs and the previously un-characterized tetraspanins T178A and T178B (Figure 1-3). In these ternary complexes, that form during early biogenesis in the ER (Figure 3A, see also below), the two tetraspanins act as structural ‘brackets’ stabilizing the bimolecular interaction between NRX and LAR-PTPRs (Figure 2). Binding of PTPRs to NRXs also occurs in the absence of the T178 proteins both *in-vitro* (Figure 2E) and *in-vivo* (Figure 3C), but with largely reduced efficiency and stability (Figure 3C). Interestingly, most of the LAR-PTPRs and T178 proteins in the adult mouse brain are present in complexes with the NRXs, while portions of NRXs were also found free of the two other constituents.

As second main outcome, our proteomic approach uncovered the NRX-T178-PTPR module(s) as central hub(s) of trans-synaptic protein networks with exquisite stability and extension as defining features. Both features were directly reflected by

the results of the forward (NRX-targeting, Table 1, Figure 1C) and reverse (*Table S4*) APs used for their exploration. Thus, the NRX-associated networks were (1) resistant to detergent-treatment, they were (2) effectively and consistently isolated from membrane preparations with multiple ABs targeting a variety of different constituents (visualized in t-SNE plots, Figures 1, 4), (3) target-interactors were co-purified with remarkably abundance (determined by quantitative MS), and, most importantly, the network (4) was affinity-purified in large multi-component 'entities' (Figures 1, 2, 4), rather than being (re)constructed post-hoc from individual isolated elements. As a remarkable feature, the isolated network entities uncovered tight trans-synaptic bonding established by the NRX-T178-PTPR module in the pre-synapse and several integral membrane proteins in the post-synapse (incl. AMPARs, LRRTs, LRFNs). Technically, isolation of these bondings imply the formation of detergent-micelles in both, pre- and post-synaptic membranes, and AB-based isolation of the resulting bi-micellar trans-synaptic protein complexes as extended high-molecular mass entities (Figure 4).

Finally, the internal structure of the identified synaptic network, as well as its detailed extensions were derived from all 'entities' isolated in extensive meAP experiments with connectivities between the individual constituents exclusively defined by specific, often mutual, co-purification(s) as a proxy for robust protein-protein interactions (Figure 5).

Functional significance for synapse operation

The NRX-T178-PTPR module-associated synaptic network in the mouse brain is made-up from an extensive number of constituents that are located in all three synaptic compartments and that are tightly interlinked by stable protein-protein interactions. Both stability and extension of this network impact the operation of the synapses in several ways, beyond the significance of individual interactions.

Most importantly, the trans-synaptic network provides a solid 'spatial organization platform' where co-operating proteins are placed in close proximity and are thus enabled to functionally interact in a reliable and timely defined manner. This is directly evident for the co-assembly of key active zone elements (Cav2, UNB13A, LIPAs) with the NRX-T178-PTPR core in the pre-synaptic membrane and the core-module mediated recruitment of several neurotransmitter receptor complexes in the post-synaptic membrane. The resulting 'nano-column' arrangement (Biederer et al., 2017; Tang et al., 2016) juxtaposes release-site(s) and effectors of neurotransmitters and thus guarantees the fastest possible and most reliable synaptic signal transduction. Remarkably, for AMPARs the trans-synaptic connectivity is realized by several molecularly distinct network strings (Figure 5) pointing to different types of synapses or different states of development and/or maturation.

Similar synergism resulting from spatial proximity may be expected for other signaling/regulatory elements identified as co-assembled constituents of the NRX-T178-PTPR network, including the GPCRs GRM4 and MGLYR, the ion channel KCMA1 or the 'synaptic organizers' LRRTs or LRFNs (DeWit et al., 2013; Lie et al.,

2018; Soler-Llavina et al., 2013; Um et al., 2016; Woo et al., 2009), but also the considerable number of proteins that have not yet been related to the two major cell adhesion molecules NRXs and LAR-PTPRs or that lack annotation of resolved primary functions (Figure 5, Table 1, *Table S4*). This includes the putative scramblase XKR6, as well as proteins T132A, ASTN1, BRNP1, LRC4B or R4RL1.

As a final aspect for network-related impact on synapse operation, the enormous 'expansion of interaction-surface' generated by the multi-protein assembly appears noteworthy. In particular in the pre-synapse, the extended network portion is expected to offer multiple sites for protein-protein interactions with lower affinity or more-readily susceptible to the detergent-treatment used in our meAP experiments. Such low(er)-affinity interactions may well include the attachment of protein assemblies/condensates resulting from phase-separation (Chen et al., 2020; Emperador-Melero et al., 2021; McDonald et al., 2020; Milovanovic et al., 2018).

Significance for synapse formation and maintenance

Key element of the characterized trans-synaptic network(s) are the complexes of NRX1-3 and LAR-PTPRs that are stably associated by the bracketing of the tetraspanins T178A and T178B. These ternary complexes link the two major presynaptic hubs established by extensive work in the past (Gomez et al., 2021; Jang et al., 2017; Sudhof, 2017; Takahashi and Craig, 2013; Takahashi et al., 2012; Yuzaki, 2018) and add an unexpected twist to the crosstalk between these two and other cell adhesion systems that is fundamental for the assembly and differentiation of synapses. Remarkably, the ternary NRX-T178-PTP complexes form early during biogenesis in the ER and are finally transported to the surface membrane as higher-mass assemblies with multiple additional interactors (Figure 3), reminiscent of the suggested active zone assembly from multi-protein precursor vesicles in the developing brain (Zhai et al., 2001).

Interestingly, tetraspanins have been reported before in immunological synapses as central players controlling spatial organization of receptors and adhesion molecules, and likewise contributions of tetraspanins to synapse formation were described in motorneuron axons in *Drosophila* (Fradkin et al., 2002). In the mammalian brain, the tight co-assembly of NRXs and LAR-type PTPRs raises new questions regarding the signaling in presynaptic terminals, at the level of NRX1 phosphorylation at tyrosine residues (Kim et al., 2020) and lipid domains (Brouwer et al., 2019). Remarkably, one of the previously unknown NRXs interactors is XKR6. While its primary function is currently unknown, the close family members XKR4 and XKR8 are lipid scramblases (Neniskyte et al., 2023; Zhang et al., 2023), pointing towards local lipid signaling at NRX-T178-PTPR-LAR membrane domains.

Most notably though, NRX-T178-PTP complexes are expected to impact the trans-synaptic recognition codes in synaptic development and plasticity. Bundling of NRXs and PTPRs substantially expands the molecular interaction codes by positioning two structurally distinct classes of synaptic adhesion cues into a single ternary molecular module. This highlights unanticipated avenues for exploring the

structural and functional underpinnings of trans-synaptic nanoscale organization and molecular recognition events at neuronal synapses. Moreover, the data provided here on the NRX-T178-PTP-associated network(s) should serve as a detailed roadmap for analyzing the role(s) of the network as an assembly platform (and the resulting spatial co-assembly/localization), as well as for studying the significance of the newly identified constituents with known and yet unknown function in synapse assembly, operation and dynamics.

Acknowledgements

We thank the Fakler and Scheiffele lab members for helpful discussions and I. Schaber for excellent technical assistance. B.F. appreciates the interactions with T. Sudhof and his efforts leading to initiation of this project.

Author Contributions

J.S., U.S. and B.F. conceived the project, S.T., J.S., P.H., M.K.K. and U.S. did all the experiments related to protein biochemistry and proteomic analyses, S.B., A.B. and S.T. performed electrophysiology, reconstruction of neurons and immune-cytochemistry, J.S., A.H. and J.vdB. performed data analysis and set up the interactive Figure 5, D.K., F.S. D.S., M.Y. and P.S. generated and characterized KO/transgenic animals, B.F. evaluated data and wrote the manuscript together with J.S. and P.S., supported by all authors.

Funding

This work was supported by grants of the Deutsche Forschungsgemeinschaft (DFG, German Research Foundation) TRR152 (project-ID 239283807), FA 332/15-1, 16-1 and 21-1 (to B.F.), the Swedish Research Council (grants 2017- 03331 and 2022-00817 to F.H.S.), the Swiss National Science Foundation (project 179432, TMAG-3-209273), the European Research Council (Advanced Grant (SPLICECODE), and the AIMS-2-TRIALS (supported by the Innovative Medicines Initiatives from the European Commission, to P.S).

Declaration of interests

The authors declare no competing interests.

Figure legends

Figure 1

meAP-MS analysis of neurexin-associated protein assemblies

(**A**), Proteomic meAP-MS approach for quantitative analysis of NRX-associated trans-synaptic protein complexes. (**B**), MS-derived protein abundance of NRX isoforms in plasma membrane-enriched fractions from adult mouse brain. Data are mean ± SD of 4 brain samples. (**C**), t-SNE plot of target normalized ratio (tnR)-values determined for all proteins (grey dots; Methods) identified in eight APs with the four distinct anti-NRX1-3 ABs with preimmunization IgGs and antiserum as negative controls and NRX1A as a reference for normalization. Right panel, extension of framed area around the target proteins (NRX1-3) highlighting a cluster of consistently co-purified proteins of mainly pre-, post- and trans-synaptic origin as indicated by the color-code. (**D**), Protein abundance determined by MS in mouse brain membrane fractions plotted against the respective protein abundances determined by MS in anti-NRX1-3 AP eluates (normalized to the abundance of NRX1A). Proteins with tight binding to the NRX-target(s) are located on the diagonal. Data are mean ± SD of two mouse brains and two independent AP eluates each. (**E**), Table summarizing a selected set of proteins specifically co-purified in APs with the indicated isoform-specific anti-NRX antibodies. Specificity was determined with target-KO (NRX1, NRX3) and IgG controls. Note that PTPRD,S and T178B are interactors of all NRX isoforms.

Figure 2

Ternary complex formation of Neurexins with LAR-type PTPRs and the tetraspanin T178B

(**A**), Native gel separation (BN-PAGE) of protein complexes in CL47-solubilized membrane fractions from adult mouse brain Western-probed for the indicated proteins. Note close co-migration of NRX1-3A, PTPRD/S and T178B as tripartite complex with an apparent molecular weight of approximately 400 kDa. Fainter signals extending to an apparent molecular mass of 1.2 MDa reflect their integration in protein networks. (**B**), tnR-plot of APs with antibodies targeting T178B and PTPRS indicate robust mutual co-purification and enrichment of NRX1-3 and a variety of pre- and post-synaptic interactors. tnR-values were determined with IgGs as a reference. Color-code of subcellular localization is indicated. (**C**), Abundance ratio determined for proteins affinity-purified in anti-HA APs from HA-Neurexin3 AS5 (GPI-anchored splice variant of NRX3, inset) mice and in anti-NRX3 APs from wild-type mice. Note that GPI-anchored NRX3 complexes lack association with presynaptic PTPRD,S, T178B and XKR6, whereas binding of extracellular ligands was maintained. Experiments were done with two distinct HA and two NRX3 ABs, values are mean of two independent experiments. (**D**), Abundance ratio for a subset of proteins affinity-purified with anti-NRX1-3 from CL91-solubilized brain membrane fractions with and without enzymatic treatment with a mixture of heparinases (I, II,

III); inset: Western-probed gel-separation indicating heparinase-mediated reduction in size of NRX3. Enzymatic activity strongly reduced co-purification of postsynaptic proteins (LRRTs, AMPAR subunits GRIA1, 2), while binding to presynaptic and extracellular/secreted interactors remained unchanged. Data are mean ± SEM of 3 experiments. (**E**), Reconstitution of ternary complexes assembled from PTPRS, NRX1A and T178B in cultured tsA cells. Specific co-purification of T178B and NRX1A with V5-tagged PTPRS in anti-V5 APs. The presence of T178B appears critical for stable complex formation with NRX1A and impacts maturation of the P-subunit of PTPRS. (**F**) Left panel, Structure of the membrane-close region of the core-module predicted by AlphaFold2-Multimer with contact sites in the transmembrane plane. Input used for AlphaFold was NRX1γ (mouse, aa 1-139, full length), PTPRS (mouse, aa 1251-1360), T178B (human, 1-294, full length). Right panel, Scheme of the ternary complex with multiple sites/domains for protein-protein interactions on both the extracellular and the cytoplasmic side of the membrane.

Figure 3

Assembly of ternary NRX-T178-PTPR module in the ER and alteration of pre-synaptic functions upon knock-down of T178B

(**A**), Abundance-mass profiles obtained for the indicated proteins by csBN-MS in CL-47 solubilized ER-enriched membrane fractions from adult mouse brain. Inset: Scheme of csBN-MS approach used (Muller et al., 2019; Schulte et al., 2023). Note close co-migration of NRX1A, PTPRD,S and T178A, B indicating their co-assembly into complexes of variable apparent mass. Values of protein abundance indicate close to stoichiometric association (see text). (**B**), Ratio of protein abundances determined by quantitative MS in membranes from cultured cortical neurons infected either with AAV driving sh-T178B expression or with control virus. Note profound alteration in the expression of distinct synaptic proteins by sh-RNA-mediated knock-down of T178B: Expression of PTPRD, S was decreased by ~40%, while essential subunits of NMDA receptors (GluN2B), Na/K-ATPase (AT1B1) and Calnexin (CALX) remained unchanged. Values are mean ± SEM of three samples of cultured neurons. Inset: Western-probed gel-separations indicating the effect of AAV:sh-T178B infection. (**C**), Alterations in PTPR and NRX complexes after knockdown of T178B. Upper panel, Input and eluates of APs with anti-PTPRS and anti-NRX1-3 APs from CL91-solubilized membrane fractions of cultured neurons transduced with two different AAV-sh-T178B viruses or control virus (WT) Western-probed with antibodies specific for NRX1-3, PTPRS,D or T178B. Lower panel, Abundance ratios determined for proteins specifically purified (and co-purified) in three anti-PTPRS and anti-NRX1-3 APs from WT and AAV-sh-T178B-2 transduced cultures by quantitative MS-analysis. Data are mean ± SD of three experiments. (**D**), Immunostaining of PTPRS in hippocampal neurons shows pronounced reduction of PTPRS expression (total and on surface). Values are mean ± SEM of 12-18 neurons of four independent cultures. (**E**), Alterations in pre-synaptic function induced by AAV-sh-T178B in hippocampal neurons of adult mice four weeks after stereotactic injection (inset, upper left). Upper right panel, Bar graph summarizing the amplitudes

of AMPAR-mediated sEPSCs and representative EPSC traces measured in whole-cell recordings in CA1 pyramidal cells (CA1 PCs) in the un-injected hemisphere (control, WT, black) and in infected (green) and non-infected (blue) PCs of the injected hemisphere (inset, lower left). Data are mean ± SEM of 19 (WT), 13 (infected) and 12 (non-infected) PCs. Lower panel, Bar graphs summarizing paired-pulse (PP) ratios determined in CA1 PCs with stimulation frequencies of 10 and 50 Hz and representative AMPAR-mediated current traces recorded at 10 Hz, color-coding of expression manipulation as in the upper panel. Data are mean ± SEM of 11 (WT), 6 (infected) and 8 (non-infected) PCs. Note the marked increase in PP-ratio of AMPAR-currents triggered by sh-T178B infected pre-synapses in both infected and non-infected CA1 PCs.

Figure 4

Comprehensive meAP-MS analyses uncover stable formation of trans-synaptic network(s)

t-SNE plots of tnR-values determined for proteins in APs with multiple ABs specifically targeting the indicated NRX interactors in pre-synapse (PTPRS, CAH10), synaptic cleft (CBLN1/2, NXPH3, TAFA1) and post-synapse (LRRT4). Insets illustrate entire space of the t-SNEs with all MS-detected proteins (for extension see Table S4), enlarged sections (framed in blue) focus on the cluster of proteins in close proximity to the respective target protein. Note that PTPRD/S, T178B and NRXs appear as central elements in all clusters, while the set of proteins specifically and consistently co-purified with the respective target protein is variable. tnR values were determined with IgGs as controls. CBLNs were purified with anti-HA ABs from transgenic HA-Cbln1 and HA-Cbln2 mouse brains with wild-type brains serving as negative control.

Figure 5

Architecture of NRX-associated protein networks projected onto the synaptic compartment

Graphical illustration of the architecture of NRX-T178-LAR-associated networks built on robust and specific (co)-purifications in APs against the indicated 30 targets (of the NRX interactome, upper panel) projected onto the synaptic compartment(s). Proteins which were specifically co-purified in individual APs with the respective target proteins (red circles) from brain membrane fractions were connected with lines in black, mutual co-purifications are indicated by red lines. Subunits/components of excitatory glutamate receptors, inhibitory $GABA_A$- or glycine receptors and presynaptic GPCRs are highlighted by filled circles in green. Note the tight and multi-dented linkage/connection between the presynaptic NRX-T178-PTPR module and the post-synapse, as well as with the synaptic cleft.

An ‘interactive’ version of Figure 5 visualizing all ‘connectivities’ determined for any selected network constituent and providing additional details on AP-data and linkages to the UniProt/SwissProt database is available online (URL).

Table 1

Interactome of native NRX1-3 (identified by meAP-MS with anti-NRX1-3 ABs)

All proteins identified by quantitative MS-analysis in the APs with the four different anti-NRX1-3 ABs were evaluated by determination of tnR-values (Methods, text) using target-unrelated ABs and pre-immunization IgGs as negative controls. All proteins with tnR-values >0.25 in APs with a least two of the four ABs were considered as specific interactors of NRXs; the entirety of these specific interactors is referred to as NRX-interactome.

Accordingly, the NRX-interactome comprises additional constituents compared to the t-SNE cluster (Figure 1C) delineating proteins that behave identical to NRX1 in APs with all four ABs.

References

Aoto, J., Foldy, C., Ilcus, S.M., Tabuchi, K., and Sudhof, T.C. (2015). Distinct circuit-dependent functions of presynaptic neurexin-3 at GABAergic and glutamatergic synapses. Nat Neurosci *18*, 997-1007.

Aoto, J., Martinelli, D.C., Malenka, R.C., Tabuchi, K., and Sudhof, T.C. (2013). Presynaptic neurexin-3 alternative splicing trans-synaptically controls postsynaptic AMPA receptor trafficking. Cell *154*, 75-88.

Bhouri, M., Morishita, W., Temkin, P., Goswami, D., Kawabe, H., Brose, N., Sudhof, T.C., Craig, A.M., Siddiqui, T.J., and Malenka, R. (2018). Deletion of LRRTM1 and LRRTM2 in adult mice impairs basal AMPA receptor transmission and LTP in hippocampal CA1 pyramidal neurons. Proc Natl Acad Sci U S A *115*, E5382-E5389.

Biederer, T., Kaeser, P.S., and Blanpied, T.A. (2017). Transcellular Nanoalignment of Synaptic Function. Neuron *96*, 680-696.

Bildl, W., Haupt, A., Muller, C.S., Biniossek, M.L., Thumfart, J.O., Huber, B., Fakler, B., and Schulte, U. (2012). Extending the dynamic range of label-free mass spectrometric quantification of affinity purifications. Mol Cell Proteomics *11*, M111 007955.

Boudkkazi, S., Brechet, A., Schwenk, J., and Fakler, B. (2014). Cornichon2 dictates the time course of excitatory transmission at individual hippocampal synapses. Neuron *82*, 848-858.

Boudkkazi, S., Schwenk, J., Nakaya, N., Brechet, A., Kollewe, A., Harada, H., Bildl, W., Kulik, A., Dong, L., Sultana, A., Zolles, G., Schulte, U., Tomarev, S., and Fakler, B. (2023). A Noelin-organized extracellular network of proteins required for constitutive and context-dependent anchoring of AMPA-receptors. Neuron *111*, 2544-2556 e2549.

Brouwer, M., Farzana, F., Koopmans, F., Chen, N., Brunner, J.W., Oldani, S., Li, K.W., van Weering, J.R., Smit, A.B., Toonen, R.F., and Verhage, M. (2019). SALM1 controls synapse development by promoting F-actin/PIP2-dependent Neurexin clustering. EMBO J *38*, e101289.

Chen, L.Y., Jiang, M., Zhang, B., Gokce, O., and Sudhof, T.C. (2017). Conditional Deletion of All Neurexins Defines Diversity of Essential Synaptic Organizer Functions for Neurexins. Neuron *94*, 611-625 e614.

Chen, X., Wu, X., Wu, H., and Zhang, M. (2020). Phase separation at the synapse. Nat Neurosci *23*, 301-310.

Chih, B., Gollan, L., and Scheiffele, P. (2006). Alternative splicing controls selective trans-synaptic interactions of the neuroligin-neurexin complex. Neuron *51*, 171-178.

Cox, J., Hein, M.Y., Luber, C.A., Paron, I., Nagaraj, N., and Mann, M. (2014). Accurate proteome-wide label-free quantification by delayed normalization and maximal peptide ratio extraction, termed MaxLFQ. Mol Cell Proteomics *13*, 2513-2526.

Cvetkovska, V., Ge, Y., Xu, Q., Li, S., Zhang, P., and Craig, A.M. (2022). Neurexin-beta Mediates the Synaptogenic Activity of Amyloid Precursor Protein. J Neurosci *42*, 8936-8947.

Dai, Y., Taru, H., Deken, S.L., Grill, B., Ackley, B., Nonet, M.L., and Jin, Y. (2006). SYD-2 Liprin-alpha organizes presynaptic active zone formation through ELKS. Nat Neurosci *9*, 1479-1487.

de Wit, J., Sylwestrak, E., O'Sullivan, M.L., Otto, S., Tiglio, K., Savas, J.N., Yates, J.R., 3rd, Comoletti, D., Taylor, P., and Ghosh, A. (2009). LRRTM2 interacts with Neurexin1 and regulates excitatory synapse formation. Neuron *64*, 799-806.

Dean, C., Scholl, F.G., Choih, J., DeMaria, S., Berger, J., Isacoff, E., and Scheiffele, P. (2003). Neurexin mediates the assembly of presynaptic terminals. Nat Neurosci *6*, 708-716.

DeWit, J., O'Sullivan, M.L., Savas, J.N., Condomitti, G., Caccese, M.C., Vennekens, K.M., Yates, J.R., and Ghosh, A. (2013). Unbiased discovery of glypican as a receptor for LRRTM4 in regulating excitatory synapse development. Neuron *79*, 696-711.

Emperador-Melero, J., Wong, M.Y., Wang, S.S.H., de Nola, G., Nyitrai, H., Kirchhausen, T., and Kaeser, P.S. (2021). PKC-phosphorylation of Liprin-alpha3 triggers phase separation and controls presynaptic active zone structure. Nat Commun *12*, 3057.

Fradkin, L.G., Kamphorst, J.T., DiAntonio, A., Goodman, C.S., and Noordermeer, J.N. (2002). Genomewide analysis of the Drosophila tetraspanins reveals a subset with similar function in the formation of the embryonic synapse. Proc Natl Acad Sci U S A *99*, 13663-13668.

Furlanis, E., Traunmuller, L., Fucile, G., and Scheiffele, P. (2019). Landscape of ribosome-engaged transcript isoforms reveals extensive neuronal-cell-class-specific alternative splicing programs. Nat Neurosci *22*, 1709-1717.

Gomez, A.M., Traunmuller, L., and Scheiffele, P. (2021). Neurexins: molecular codes for shaping neuronal synapses. Nat Rev Neurosci *22*, 137-151.

Graf, E.R., Zhang, X., Jin, S.X., Linhoff, M.W., and Craig, A.M. (2004). Neurexins induce differentiation of GABA and glutamate postsynaptic specializations via neuroligins. Cell *119*, 1013-1026.

Han, K.A., Kim, Y.J., Yoon, T.H., Kim, H., Bae, S., Um, J.W., Choi, S.Y., and Ko, J. (2020). LAR-RPTPs Directly Interact with Neurexins to Coordinate Bidirectional Assembly of Molecular Machineries. J Neurosci *40*, 8438-8462.

Hauser, D., Behr, K., Konno, K., Schreiner, D., Schmidt, A., Watanabe, M., Bischofberger, J., and Scheiffele, P. (2022). Targeted proteoform mapping uncovers specific Neurexin-3 variants required for dendritic inhibition. Neuron *110*, 2094-2109 e2010.

Ito-Ishida, A., Miyazaki, T., Miura, E., Matsuda, K., Watanabe, M., Yuzaki, M., and Okabe, S. (2012). Presynaptically released Cbln1 induces dynamic axonal structural changes by interacting with GluD2 during cerebellar synapse formation. Neuron *76*, 549-564.

Jang, S., Lee, H., and Kim, E. (2017). Synaptic adhesion molecules and excitatory synaptic transmission. Curr Opin Neurobiol *45*, 45-50.

Khalaj, A.J., Sterky, F.H., Sclip, A., Schwenk, J., Brunger, A.T., Fakler, B., and Sudhof, T.C. (2020). Deorphanizing FAM19A proteins as pan-neurexin ligands with an unusual biosynthetic binding mechanism. J Cell Biol *219*, e202004164.

Kim, K., Shin, W., Kang, M., Lee, S., Kim, D., Kang, R., Jung, Y., Cho, Y., Yang, E., Kim, H., Bae, Y.C., and Kim, E. (2020). Presynaptic PTPsigma regulates postsynaptic NMDA receptor function through direct adhesion-independent mechanisms. Elife *9*.

Ko, J., Zhang, C., Arac, D., Boucard, A.A., Brunger, A.T., and Sudhof, T.C. (2009). Neuroligin-1 performs neurexin-dependent and neurexin-independent functions in synapse validation. EMBO J *28*, 3244-3255.

Kocylowski, M.K., Aypek, H., Bildl, W., Helmstadter, M., Trachte, P., Dumoulin, B., Wittosch, S., Kuhne, L., Aukschun, U., Teetzen, C., Kretz, O., Gaal, B., Kulik, A., Antignac, C., Mollet, G., Kottgen, A., Gocmen, B., Schwenk, J., Schulte, U., Huber, T.B.*, et al.* (2022). A slit-diaphragm-associated protein network for dynamic control of renal filtration. Nat Commun *13*, 6446.

Kollewe, A., Chubanov, V., Tseung, F.T., Correia, L., Schmidt, E., Rossig, A., Zierler, S., Haupt, A., Muller, C.S., Bildl, W., Schulte, U., Nicke, A., Fakler, B., and Gudermann, T. (2021). The molecular appearance of native TRPM7 channel complexes identified by high-resolution proteomics. Elife *10*.

Kollewe, A., Schwarz, Y., Oleinikov, K., Raza, A., Haupt, A., Wartenberg, P., Wyatt, A., Boehm, U., Ectors, F., Bildl, W., Zolles, G., Schulte, U., Bruns, D., Flockerzi, V., and Fakler, B. (2022). Subunit composition, molecular environment, and activation of native TRPC channels encoded by their interactomes. Neuron *110*, 4162-4175 e4167.

Kurshan, P.T., Merrill, S.A., Dong, Y., Ding, C., Hammarlund, M., Bai, J., Jorgensen, E.M., and Shen, K. (2018). gamma-Neurexin and Frizzled Mediate Parallel Synapse Assembly Pathways Antagonized by Receptor Endocytosis. Neuron *100*, 150-166 e154.

Laboute, T., Zucca, S., Holcomb, M., Patil, D.N., Garza, C., Wheatley, B.A., Roy, R.N., Forli, S., and Martemyanov, K.A. (2023). Orphan receptor GPR158 serves as a metabotropic glycine receptor: mGlyR. Science *379*, 1352-1358.

Li, B., Brusman, L., Dahlka, J., and Niswander, L.A. (2022). TMEM132A ensures mouse caudal neural tube closure and regulates integrin-based mesodermal migration. Development *149*.

Li, Y., Zhang, P., Choi, T.Y., Park, S.K., Park, H., Lee, E.J., Lee, D., Roh, J.D., Mah, W., Kim, R., Kim, Y., Kwon, H., Bae, Y.C., Choi, S.Y., Craig, A.M., and Kim, E. (2015). Splicing-Dependent Trans-

synaptic SALM3-LAR-RPTP Interactions Regulate Excitatory Synapse Development and Locomotion. Cell Rep *12*, 1618-1630.

Lie, E., Li, Y., Kim, R., and Kim, E. (2018). SALM/Lrfn Family Synaptic Adhesion Molecules. Frontiers in molecular neuroscience *11*, 105-105.

Marco de la Cruz, B., Campos, J., Molinaro, A., Xie, X., Jin, G., Wei, Z., Acuna, C., and Sterky, F.H. (2024). Liprin-alpha proteins are master regulators of human presynapse assembly. Nat Neurosci *27*, 629-642.

Matsuda, K., and Yuzaki, M. (2011). Cbln family proteins promote synapse formation by regulating distinct neurexin signaling pathways in various brain regions. Eur J Neurosci *33*, 1447-1461.

McDonald, N.A., Fetter, R.D., and Shen, K. (2020). Assembly of synaptic active zones requires phase separation of scaffold molecules. Nature *588*, 454-458.

McInnes, L., Healy, J., Saul, N., and Großberger, L. (2018). UMAP: Uniform Manifold Approximation and Projection. J Open Source Software *3*, 861.

Milovanovic, D., Wu, Y., Bian, X., and De Camilli, P. (2018). A liquid phase of synapsin and lipid vesicles. Science *361*, 604-607.

Missler, M., and Sudhof, T.C. (1998). Neurexophilins form a conserved family of neuropeptide-like glycoproteins. J Neurosci *18*, 3630-3638.

Missler, M., Zhang, W., Rohlmann, A., Kattenstroth, G., Hammer, R.E., Gottmann, K., and Sudhof, T.C. (2003). Alpha-neurexins couple Ca2+ channels to synaptic vesicle exocytosis. Nature *423*, 939-948.

Montoliu-Gaya, L., Tietze, D., Kaminski, D., Mirgorodskaya, E., Tietze, A.A., and Sterky, F.H. (2021). CA10 regulates neurexin heparan sulfate addition via a direct binding in the secretory pathway. EMBO Rep *22*, e51349.

Muhammad, K., Reddy-Alla, S., Driller, J.H., Schreiner, D., Rey, U., Bohme, M.A., Hollmann, C., Ramesh, N., Depner, H., Lutzkendorf, J., Matkovic, T., Gotz, T., Bergeron, D.D., Schmoranzer, J., Goettfert, F., Holt, M., Wahl, M.C., Hell, S.W., Scheiffele, P., Walter, A.M*., et al.* (2015). Presynaptic spinophilin tunes neurexin signalling to control active zone architecture and function. Nat Commun *6*, 8362.

Muller, C.S., Bildl, W., Klugbauer, N., Haupt, A., Fakler, B., and Schulte, U. (2019). High-Resolution Complexome Profiling by Cryoslicing BN-MS Analysis. J Vis Exp.

Muller, C.S., Haupt, A., Bildl, W., Schindler, J., Knaus, H.G., Meissner, M., Rammner, B., Striessnig, J., Flockerzi, V., Fakler, B., and Schulte, U. (2010). Quantitative proteomics of the Cav2 channel nano-environments in the mammalian brain. Proc Natl Acad Sci U S A *107*, 14950-14957.

Neniskyte, U., Kuliesiute, U., Vadisiute, A., Jevdokimenko, K., Coletta, L., Deivasigamani, S., Pamedytyte, D., Daugelaviciene, N., Dabkeviciene, D., Perlas, E., Bali, A., Basilico, B., Gozzi, A., Ragozzino, D., and Gross, C.T. (2023). Phospholipid scramblase Xkr8 is required for developmental axon pruning via phosphatidylserine exposure. EMBO J *42*, e111790.

Nguyen, T.M., Schreiner, D., Xiao, L., Traunmuller, L., Bornmann, C., and Scheiffele, P. (2016). An alternative splicing switch shapes neurexin repertoires in principal neurons versus interneurons in the mouse hippocampus. Elife *5*.

Nozawa, K., Hayashi, A., Motohashi, J., Takeo, Y.H., Matsuda, K., and Yuzaki, M. (2018). Cellular and Subcellular Localization of Endogenous Neuroligin-1 in the Cerebellum. Cerebellum *17*, 709-721.

Nozawa, K., Sogabe, T., Hayashi, A., Motohashi, J., Miura, E., Arai, I., and Yuzaki, M. (2022). In vivo nanoscopic landscape of neurexin ligands underlying anterograde synapse specification. Neuron *110*, 3168-3185 e3168.

Owald, D., Khorramshahi, O., Gupta, V.K., Banovic, D., Depner, H., Fouquet, W., Wichmann, C., Mertel, S., Eimer, S., Reynolds, E., Holt, M., Aberle, H., and Sigrist, S.J. (2012). Cooperation of Syd-1 with Neurexin synchronizes pre- with postsynaptic assembly. Nat Neurosci *15*, 1219-1226.

Ozel, M.N., Kulkarni, A., Hasan, A., Brummer, J., Moldenhauer, M., Daumann, I.M., Wolfenberg, H., Dercksen, V.J., Kiral, F.R., Weiser, M., Prohaska, S., von Kleist, M., and Hiesinger, P.R. (2019). Serial

Synapse Formation through Filopodial Competition for Synaptic Seeding Factors. Dev Cell *50*, 447-461 e448.

Park, H., Choi, Y., Jung, H., Kim, S., Lee, S., Han, H., Kweon, H., Kang, S., Sim, W.S., Koopmans, F., Yang, E., Kim, H., Smit, A.B., Bae, Y.C., and Kim, E. (2020). Splice-dependent trans-synaptic PTPdelta-IL1RAPL1 interaction regulates synapse formation and non-REM sleep. EMBO J *39*, e104150.

Roppongi, R.T., Dhume, S.H., Padmanabhan, N., Silwal, P., Zahra, N., Karimi, B., Bomkamp, C., Patil, C.S., Champagne-Jorgensen, K., Twilley, R.E., Zhang, P., Jackson, M.F., and Siddiqui, T.J. (2020). LRRTMs Organize Synapses through Differential Engagement of Neurexin and PTPsigma. Neuron *106*, 108-125 e112.

Sainburg, T., McInnes, L., and Gentner, T.Q. (2021). Parametric UMAP Embeddings for Representation and Semisupervised Learning. Neural Comput *33*, 2881-2907.

Saunders, A., Macosko, E.Z., Wysoker, A., Goldman, M., Krienen, F.M., de Rivera, H., Bien, E., Baum, M., Bortolin, L., Wang, S., Goeva, A., Nemesh, J., Kamitaki, N., Brumbaugh, S., Kulp, D., and McCarroll, S.A. (2018). Molecular Diversity and Specializations among the Cells of the Adult Mouse Brain. Cell *174*, 1015-1030 e1016.

Schmidt, N., Kollewe, A., Constantin, C.E., Henrich, S., Ritzau-Jost, A., Bildl, W., Saalbach, A., Hallermann, S., Kulik, A., Fakler, B., and Schulte, U. (2017). Neuroplastin and Basigin Are Essential Auxiliary Subunits of Plasma Membrane Ca(2+)-ATPases and Key Regulators of Ca(2+) Clearance. Neuron *96*, 827-838 e829.

Schreiner, D., Nguyen, T.M., Russo, G., Heber, S., Patrignani, A., Ahrne, E., and Scheiffele, P. (2014). Targeted combinatorial alternative splicing generates brain region-specific repertoires of neurexins. Neuron *84*, 386-398.

Schulte, U., den Brave, F., Haupt, A., Gupta, A., Song, J., Muller, C.S., Engelke, J., Mishra, S., Martensson, C., Ellenrieder, L., Priesnitz, C., Straub, S.P., Doan, K.N., Kulawiak, B., Bildl, W., Rampelt, H., Wiedemann, N., Pfanner, N., Fakler, B., and Becker, T. (2023). Mitochondrial complexome reveals quality-control pathways of protein import. Nature *614*, 153-159.

Schwenk, J., Boudkkazi, S., Kocylowski, M.K., Brechet, A., Zolles, G., Bus, T., Costa, K., Kollewe, A., Jordan, J., Bank, J., Bildl, W., Sprengel, R., Kulik, A., Roeper, J., Schulte, U., and Fakler, B. (2019). An ER Assembly Line of AMPA-Receptors Controls Excitatory Neurotransmission and Its Plasticity. Neuron *104*, 680-692 e689.

Schwenk, J., Harmel, N., Brechet, A., Zolles, G., Berkefeld, H., Muller, C.S., Bildl, W., Baehrens, D., Huber, B., Kulik, A., Klocker, N., Schulte, U., and Fakler, B. (2012). High-resolution proteomics unravel architecture and molecular diversity of native AMPA receptor complexes. Neuron *74*, 621-633.

Schwenk, J., Metz, M., Zolles, G., Turecek, R., Fritzius, T., Bildl, W., Tarusawa, E., Kulik, A., Unger, A., Ivankova, K., Seddik, R., Tiao, J.Y., Rajalu, M., Trojanova, J., Rohde, V., Gassmann, M., Schulte, U., Fakler, B., and Bettler, B. (2010). Native GABA(B) receptors are heteromultimers with a family of auxiliary subunits. Nature *465*, 231-235.

Schwenk, J., Perez-Garci, E., Schneider, A., Kollewe, A., Gauthier-Kemper, A., Fritzius, T., Raveh, A., Dinamarca, M.C., Hanuschkin, A., Bildl, W., Klingauf, J., Gassmann, M., Schulte, U., Bettler, B., and Fakler, B. (2016). Modular composition and dynamics of native GABAB receptors identified by high-resolution proteomics. Nat Neurosci *19*, 233-242.

Sclip, A., and Sudhof, T.C. (2023). Combinatorial expression of neurexins and LAR-type phosphotyrosine phosphatase receptors instructs assembly of a cerebellar circuit. Nat Commun *14*, 4976.

Seigneur, E., and Sudhof, T.C. (2017). Cerebellins are differentially expressed in selective subsets of neurons throughout the brain. J Comp Neurol *525*, 3286-3311.

Siddiqui, T.J., Pancaroglu, R., Kang, Y., Rooyakkers, A., and Craig, A.M. (2010). LRRTMs and neuroligins bind neurexins with a differential code to cooperate in glutamate synapse development. J Neurosci *30*, 7495-7506.

Soler-Llavina, G.J., Arstikaitis, P., Morishita, W., Ahmad, M., Sudhof, T.C., and Malenka, R.C. (2013). Leucine-rich repeat transmembrane proteins are essential for maintenance of long-term potentiation. Neuron *79*, 439-446.

Sterky, F.H., Trotter, J.H., Lee, S.J., Recktenwald, C.V., Du, X., Zhou, B., Zhou, P., Schwenk, J., Fakler, B., and Sudhof, T.C. (2017). Carbonic anhydrase-related protein CA10 is an evolutionarily conserved pan-neurexin ligand. Proc Natl Acad Sci U S A *114*, E1253-E1262.

Sudhof, T.C. (2017). Synaptic Neurexin Complexes: A Molecular Code for the Logic of Neural Circuits. Cell *171*, 745-769.

Takahashi, H., and Craig, A.M. (2013). Protein tyrosine phosphatases PTPdelta, PTPsigma, and LAR: presynaptic hubs for synapse organization. Trends Neurosci *36*, 522-534.

Takahashi, H., Katayama, K., Sohya, K., Miyamoto, H., Prasad, T., Matsumoto, Y., Ota, M., Yasuda, H., Tsumoto, T., Aruga, J., and Craig, A.M. (2012). Selective control of inhibitory synapse development by Slitrk3-PTPdelta trans-synaptic interaction. Nat Neurosci *15*, 389-398, S381-382.

Tang, A.H., Chen, H., Li, T.P., Metzbower, S.R., MacGillavry, H.D., and Blanpied, T.A. (2016). A trans-synaptic nanocolumn aligns neurotransmitter release to receptors. Nature *536*, 210-214.

Treutlein, B., Gokce, O., Quake, S.R., and Sudhof, T.C. (2014). Cartography of neurexin alternative splicing mapped by single-molecule long-read mRNA sequencing. Proc Natl Acad Sci U S A *111*, E1291-1299.

Trotter, J.H., Hao, J., Maxeiner, S., Tsetsenis, T., Liu, Z., Zhuang, X., and Sudhof, T.C. (2019). Synaptic neurexin-1 assembles into dynamically regulated active zone nanoclusters. J Cell Biol *218*, 2677-2698.

Trovo, L., Kouvaros, S., Schwenk, J., Fernandez-Fernandez, D., Fritzius, T., Rem, P.D., Fruh, S., Gassmann, M., Fakler, B., Bischofberger, J., and Bettler, B. (2024). Synaptotagmin-11 facilitates assembly of a presynaptic signaling complex in post-Golgi cargo vesicles. EMBO Rep *25*, 2610-2634.

Uemura, T., Lee, S.J., Yasumura, M., Takeuchi, T., Yoshida, T., Ra, M., Taguchi, R., Sakimura, K., and Mishina, M. (2010). Trans-synaptic interaction of GluRdelta2 and Neurexin through Cbln1 mediates synapse formation in the cerebellum. Cell *141*, 1068-1079.

Ullrich, B., Ushkaryov, Y.A., and Sudhof, T.C. (1995). Cartography of neurexins: more than 1000 isoforms generated by alternative splicing and expressed in distinct subsets of neurons. Neuron *14*, 497-507.

Um, J.W., Choi, T.Y., Kang, H., Cho, Y.S., Choii, G., Uvarov, P., Park, D., Jeong, D., Jeon, S., Lee, D., Kim, H., Lee, S.H., Bae, Y.C., Choi, S.Y., Airaksinen, M.S., and Ko, J. (2016). LRRTM3 Regulates Excitatory Synapse Development through Alternative Splicing and Neurexin Binding. Cell Rep *14*, 808-822.

Ushkaryov, Y.A., Petrenko, A.G., Geppert, M., and Sudhof, T.C. (1992). Neurexins: synaptic cell surface proteins related to the alpha-latrotoxin receptor and laminin. Science *257*, 50-56.

Van Rossum, G., and Drake Jr, F. (1995). Python reference manual (Centrum voor Wiskunde en Informatica Amsterdam).

Wentzel, C., Sommer, J.E., Nair, R., Stiefvater, A., Sibarita, J.B., and Scheiffele, P. (2013). mSYD1A, a mammalian synapse-defective-1 protein, regulates synaptogenic signaling and vesicle docking. Neuron *78*, 1012-1023.

Wong, M.Y., Liu, C., Wang, S.S.H., Roquas, A.C.F., Fowler, S.C., and Kaeser, P.S. (2018). Liprin-alpha3 controls vesicle docking and exocytosis at the active zone of hippocampal synapses. Proc Natl Acad Sci U S A *115*, 2234-2239.

Woo, J., Kwon, S.K., Choi, S., Kim, S., Lee, J.R., Dunah, A.W., Sheng, M., and Kim, E. (2009). Trans-synaptic adhesion between NGL-3 and LAR regulates the formation of excitatory synapses. Nature Neuroscience *12*, 428-437.

Yan, Q., Weyn-Vanhentenryck, S.M., Wu, J., Sloan, S.A., Zhang, Y., Chen, K., Wu, J.Q., Barres, B.A., and Zhang, C. (2015). Systematic discovery of regulated and conserved alternative exons in the mammalian brain reveals NMD modulating chromatin regulators. Proc Natl Acad Sci U S A *112*, 3445-3450.

Yuzaki, M. (2018). Two Classes of Secreted Synaptic Organizers in the Central Nervous System. Annu Rev Physiol *80*, 243-262.

Zhai, R.G., Vardinon-Friedman, H., Cases-Langhoff, C., Becker, B., Gundelfinger, E.D., Ziv, N.E., and Garner, C.C. (2001). Assembling the presynaptic active zone: a characterization of an active one precursor vesicle. Neuron *29*, 131-143.

Zhang, P., Lu, H., Peixoto, R.T., Pines, M.K., Ge, Y., Oku, S., Siddiqui, T.J., Xie, Y., Wu, W., Archer-Hartmann, S., Yoshida, K., Tanaka, K.F., Aricescu, A.R., Azadi, P., Gordon, M.D., Sabatini, B.L., Wong, R.O.L., and Craig, A.M. (2018). Heparan Sulfate Organizes Neuronal Synapses through Neurexin Partnerships. Cell *174*, 1450-1464 e1423.

Zhang, P., Maruoka, M., Suzuki, R., Katani, H., Dou, Y., Packwood, D.M., Kosako, H., Tanaka, M., and Suzuki, J. (2023). Extracellular calcium functions as a molecular glue for transmembrane helices to activate the scramblase Xkr4. Nat Commun *14*, 5592.

Methods

EXPERIMENTAL MODEL AND SUBJECT DETAILS

Generation of knockout/knockin animals

HA-NRX1 knock-in mice (Sterky et al., 2017; Trotter et al., 2019), NRX3 knock-out (generation as in *Figure S5*), NRX3 AS5 HA/HA (Hauser et al., 2022), HA-Nlgn1 knock-in mice (Nozawa et al., 2018) and HA-Cbln1 (Nozawa et al., 2022) were generated as described previously. NRX3 knock-outs (*Figure S5*) were generated by inserting a gene-trap after the first exon common to both α- and β-isoforms, using homology-arms PCR-amplified from C57BL/6 genomic BAC clones. The targeting vector, containing an SDA (self-deletion anchor)-flanked neomycin resistance cassette, and a DTA (diphtheria toxin fragment A)-cassette for negative selection, was electroporated into C57BL/6 ES cells (Cyagen). G418-resistant clones were isolated, verified by PCR and Southern Blot and injected into C57Bl/6 albino embryos (Cyagen). Following germline transmission and deletion of the neomycin cassette, heterozygotes were intercrossed to generate homozygous Nrxn3$^{gt/gt}$ offspring and wildtype littermates. HA-Cbln2 knock-in mice were generated following the approach described in (Nozawa et al., 2022). Briefly, superovulated B6D2F1 female mice (8 weeks old) were mated with B6D2F1 males and zygotes were collected from the oviducts at embryonic day 0.5 and incubated with SpCas9 protein (250ng/µl; PNA Bio, CA, USA), Cbln2-crRNA (5pmol/µl, 5'-CGUAAGGGCUCAGAACGACAGUUUUAGAGCUAUGCUGUUUUG-3'), trans-activating RNA (5pmol/µl; Fasmac, Kanagawa, Japan) and 131-bases single-strand donor DNA oligo(500ng/µl; 5'-TGGCCCTGCTGTTGCTGCTGCTG-CCCGCCTGCTGCCCCGTAAGGGCTCAGTACCCATACGACGTGCCAGACTACG CTAACGACACGGAGCCCATCGTGCTAGAGGGCAAGTGCCTGGTAGTGTGCGA TTCC-3'; Integrated DNA Technologies, IA, USA) at 37℃ for 15 min. Electroporation was performed using platinum block electrodes (150 mA, 2 pulses, 1msecON+100msecOFF, GE-101, BEX, Tokyo, Japan) connected to CUY21EDIT II (BEX). Zygotes were incubated to the two-cell stage and transferred into oviducts of presudo-pregnant ICR females. To investigate CRISPR/Cas9-mediated mutation in the Cbln2 gene, the genomic DNA was prepared from mouse tales and the genomic regions flanking the gRNA target were amplified by PCR using specific primers: Fwd (5'-ACTTGTTCCCCTTCTACCTGCC-3') and Rev (5'-GTACGGTTGCTCA-TCTCTGACG-3'). Knockouts for CA10 (*Car10*) were generated by breeding *Car11*^{em1Sud} *Car10*^{em1Sud}*/J* mice (Jackson Laboratories #031998) to C57Bl/6 and subsequently intercrossing *Car10*^{em1Sud} heterozygotes to obtain homozygous offspring and wildtype littermates.

Molecular Biology

The cDNAs used were all verified by sequencing. T178B carrying a Myc-Flag Tag at the C-terminus was obtained from Origene (Klon RR216273) and subcloned into pcDNA3.1. PTPRS (GenBank: BC083188.1) was modified with a V5-tag at the C-

terminus. HA-tagged NRX1A subcloned into pCAG was obtained from Addgene (#58622). HA-tagged constructs for expression of NRX3A and NRX3A AS5 were as described in (Hauser et al., 2022).

Biochemistry and Cell Biology

Membrane preparation from mouse brain

Whole brains were dissected from adult C57BL/6 WT mice (Charles River) or genetically modified mice. Brains were cut into pieces and homogenized in 10 mM Tris/HCl buffer (pH 7.5) supplemented with 320 mM sucrose, 1.5 mM $MgCl_2$, 1 mM EGTA, 1 mM Iodoacetamide and protease inhibitors (Aprotinin, Leupeptin, Pepstatin A, PMSF) using a loose pestle in a 15 ml dounce tissue grinder. Supernatants of centrifugations (4 min, 1,000xg) were collected in tubes for ultracentrifugation. Homogenization procedure was repeated with the remaining tissue remnants in order to increase the yield. Combined supernatants were ultracentrifuged (200,000 x g, for 20 min). The resulting pellet were homogenized with dounce tissue grinder (tight pestle) in hypotonic lysis buffer (10 mM Tris/HCl (pH 7,4) and protease inhibitors) and incubated on ice for 20 minutes. After ultracentrifugation (200,000 x g, for 30 min) membrane pellets were resuspended in 8 ml of 0.5 M sucrose / 20 mM Tris/HCl (pH 7.4) and homogenized. Suspension were filled in thin layer ultracentrifugation tubes and underlaid with 12 ml 0.5 M sucrose / 20 mM Tris/HCl (pH 7.4) and 18 ml 1.3 M sucrose / 20 mM Tris/HCl (pH 7.4) and subjected to ultracentrifugation (180,000 x g, for 30 min, SW-32, Beckman). The membrane phase between the two sucrose layers was harvested and diluted with 20 mM Tris/HCl (pH 7.4) to wash out sucrose. Ultracentrifugation (200,000 x g, for 30 min) was used to pellet the membranes which were then resuspended in a small volume of 20 mM Tris/HCl (pH 7.4) to reach concentrations about 10 mg/ml. Protein concentration were determined by Bradford assay and samples were aliquoted and shock-frozen in liquid nitrogen.

Preparation of ER-enriched mouse brain fraction

The isolation of ER-enriched membrane fractions from mouse brain was essentially done as described in (Schwenk et al., 2019). For complexome profiling (csBN-MS) was adjusted as follows. Whole brains of C57BL/6 WT mice were dissected and homogenised in 0.25 M SHE buffer (10 mM HEPES (pH 7.5), 1 mM EDTA, 2 mM PMSF, protease inhibitors see above) first using a loose pestle in a 15 mL dounce tissue grinder and then processed in a cell cracker (8.002 mm ball, 2 passages, 2 rounds per turn). Homogenates were centrifuged at 600 x g for 5 min. The supernatant was collected and the pellet was washed with homogenization buffer. Combined supernatants were centrifuged again (600 x g for 10 min). The resulting supernatant was then subjected to ultracentrifugation (200,000 x g, for 30 min). The pellet (P200) was homogenized in hypotonic buffer (5 mM HEPES (pH 7.5) containing 1 mM PMSF and protease inhibitors), left to incubate for 1 hour on ice with agitation and subsequently centrifuged at 12,000 x g, for 15 min. The supernatant was collected and placed on top of a two layer density gradient (8.3%

(0.25 M) and 23% buffered sucrose). After ultracentrifugation (135,000 x g for 1 h) the interface between 8,3% and 23% sucrose layers was harvested, diluted in 20 mM Tris/HCl (pH 7.5), and pelleted (200,000 x g, for 25 min). The ER-enriched membrane vesicles were resuspended in 20 mM Tris/HCl (pH 7.5). Protein concentrations were determined by Bradford assay.

Covalent coupling of antibodies

For APs, selected ABs were covalently coupled to magnetic Dynabeads ™ Protein A or Dynabeads ™ Protein G. Selected ABs were diluted in PBST (1 µg of AB with 10 µl filtered PBST) and incubated with Dynabeads™ Protein A or G, for 1 h (4 µl Dynabeads per µg of coupled AB). Subsequently, ABs coupled to beads were crosslinked for 30 min by addition of 20 mM Dimethyl pimelimidate dihydrochloride in pre-filtered 100 mM sodium borate, 0.05% Tween (pH 9). Reactions were blocked by adding 200 mM ethanolamine, 0.05% Tween (pH 8). Non-crosslinked ABs were washed off by incubation for 2 x 5 minutes with 100 mM Glycine in 0.05% Tween (pH 3). After 3 x washing steps with PBST coupled ABs were used for APs or stored for short periods at 4°C.

Antibody based affinity-purifications

Protein complexes in plasma membrane and ER enriched fractions from mouse brains were solubilised with ComplexioLyte 91 (CL-91) or ComplexioLyte 47 (CL-47, Logopharm GmbH) supplemented with 1 mM $CaCl_2$ (and protease inhibitors (Aprotinin, Leupeptin, Pepstatin A, PMSF)). After clearing by ultracentrifugation (10 min, 125,000 x g) solubilisates (1-1.5 mg) were incubated for 2 hours with 10-15 µg ABs pre-coupled to protein A Dynabeads . APs and respective control experiments used to calculate the specificity of interactions (see tnR-ratio calculation below), were performed with identical settings. Target APs were replicated by using different batches of membrane fractions generated from WT mouse brains (as described above). AP experiments with genetically modified brain tissue as source material (NLGN1-HA, CBLN1-HA, CBLN2-HA, Nrx1-HA, NRX3-KO) were done in parallel with controls obtained from age-matched WT littermates. Details of the experimental series are described in Figure legends and are given in Tables S1-4. The following antibodies were used for APs: *anti-Nrx1-3* (Millipore, #ABN161-I), *anti-Nrx1-3* (AB generation by LifeTein, #RB2987, rabbit, epitope: mouse NRX3A aa 1523-1571); *anti-Nrx1-3* (Synaptic Systems, #175003), *anti-Nrx1-3* (AB generation by AbFrontier, #3-4-rb1, rabbit, epitope: mouse NRX3A aa 1471-1491), *anti-Nrx1* (Synaptic Systems, #175103), *anti-Nrx1* (RnD Systems, #AF4524), *anti-Nrx2* (AB generation by LifeTein, #RB4227, rabbit, epitope: mouse NRX2A aa 266-282), *anti-Nrx2* (AB generation by LifeTein, #RB4226, rabbit, epitope: mouse NRX2A aa 1459-1476), *anti-Nrx2* (AB generation by LifeTein, rabbit, #RB4225, epitope: mouse NRX2A aa 1459-1476), *anti-Nrx2* (Abcam, #ab34245), *anti-Nrx3* (AB generation by AbFrontier, rabbit, #3-1-rb1, epitope: mouse NRX3A aa 1349-1368), *anti-Nrx3* (Synaptic Systems, #175303), *anti-Nrx3* (AB generation by AbFrontier, rabbit, #3-2-rb1, epitope: mouse NRX3A aa 1377-1397), *anti-Nrx3* (RnD Systems, #AF5269),

anti-Nrx3 (AB generation by AbFrontier, rabbit, #3-2-rb2, epitope: mouse NRX3A aa 1377-1397), anti-T178B (AB generation by LifeTein, rabbit, #RB4235, epitope: mouse T178B aa 273-294), anti-T178B (AB generation by AmsBio, rabbit, #RB3967, epitope: mouse T178B aa 273-294), anti-HA (Roche, #11867423001), anti-HA (Thermo Fisher, #26183), anti-PTPRS (RnD Systems, #AF3430), anti-PTPRS (MediMabs, #MM-0020-P), anti-PTPRS (Invitrogen, #PA5-47487), anti-CAH10 (RnD Systems, #MAB2189), anti-CAH10 (raised against recombinant CAH10 ((Montoliu-Gaya et al., 2021), rabbit, #Hadlai), anti-CAH10 (raised against recombinant CAH10 (Montoliu-Gaya et al., 2021), rabbit, #Habeba), anti-CAC1A (FrontierInstitute, #GP-Af810), anti-CAC1E (Alomone, #ACC-006), anti-TAFA1 (RnD Systems, #AF5154), anti-TAFA2 (RnD Systems, #AF4179), anti-NXPH1 (RnD Systems, #AF4208), anti-NXPH3 (RnD Systems, #AF5098), anti-LRRT4 (Neuromab, #75-261), anti-LRRT4 (AbFrontier, rabbit, #C1, raised against mouse LRRT4 aa 548-568), anti-LRRT4 (RnD Systems, #AF5377), anti-A4 (Abgent, #ABIN1741750), anti-A4 (Sigma, #A8717), anti-GBRA1 (Synaptic Systems, #224203), anti-GBRG (Synaptic Systems, #224003), anti-RTN4R (RnD Systems, #AF1440), anti-LRRT1 (MerckMillipore, #ABN642), anti-LRRT2 (NeuroMab, #75-364), anti-GRM4 (Abcam, #ab53088), anti-GRM4 (Abcam, #ab184302), anti-GRM4 (Bioworld, #BS1144), anti-NLGN2 (Synaptic Systems, #129511), anti-NLGN3 (NeuroMab, #75-158), anti-Syt11 (Synaptic Systems, #270003), anti-XKR6 (AB generation by AmsBio, rabbit, #RB3961, epitope: mouse XKR6 aa 85-102), anti-XKR6 (AB generation by AmsBio, rabbit, #RB3962, epitope: mouse XKR6 aa 85-102), anti-XKR6 (Signalway Antibody, #42864), IgG (Millipore, #12-370), rabbit pre-immune-sera (LifeTein).

Enzymatic removal of heparan sulfates (HS)

Impact of HS on NRX-interactions was assessed by APs after pre-treatment with a heparinase cocktail. For this purpose, plasma-membrane enriched fractions from mouse brain were incubated for 1 h with a mix of Heparinases (2 Units/ml mix of Heparinase I (Sigma-Aldrich, H2519), Heparinase II (Sigma-Aldrich, H6512) and Heparinase III (Sigma-Aldrich, H8891)) diluted in reaction buffer (20 mM Tris/HCl (pH 7.4), 100 mM NaCl, 2 mM $CaCl_2$ and a mix of protease inhibitors (Aprotinin, Leupeptin, Pepstatin A). As control, membranes processed in parallel without additions of enzymes were used. After enzymatic treatment, membranes were pelleted by ultracentrifugation (100,000 x g for 10 min, 4°C) and supernatants were removed. Subsequently membranes were solubilized with CL-91 and processed as described above for APs with a mixture of anti-Nrx1-3 antibodies (anti-Nrx1, #ABN161, Millipore; anti-Nrx1, Synaptic Systems, #175103) and subjected to MS-analysis.

Complex reconstitution in tsA cells

tsA201 cells were used for transient co-expression of V5-tagged PTPRS, T178B-Myc-FLAG, NRX1A-HA and NRX3A-HA. Cells were cultivated in high glucose Dulbecco's Minimal Eagles Medium (DMEM), supplemented with 0.45% glucose,

10% (v/v) FCS, 1% (v/v) Penicillin/Streptomycin and 1% (v/v) HEPES. Two days after PEI (Polysciences)-mediated transfection cells were washed with PBS and released by cell scrapers in 20 mM Tris/HCl (pH 7,4), 150 mM NaCl, 1 mM EDTA, 1 mM PMSF and protease inhibitors. Cells were centrifuged (150,000xg, 10 min) and lysed in 20 mM Tris/HCl (pH 7,4) by ultrasonication (5s-pulses, output 50%). Membrane vesicles were pelleted by ultracentrifugation (150,000xg, 10 min) and resuspended to homogeneity in 20 mM Tris/HCl (pH 7.4). Protein concentrations of membrane suspensions were determined by Bradford assay and aliquots shock-frozen in liquid nitrogen and stored at -80°C. Experiments were performed in parallel. For each AP, 0.5 mg membrane fractions were incubated for 30 min in CL-91 (supplemented with 1 mM PMSF, 1 mM Iodoacetamide). After clearing by ultracentrifugation (125,000xg, 10 min), solubilisates were incubated for 2 hours with 3 µg of coupled ABs (V5, BioRad, #MCA1360) or 40 µl anti-FLAG affinity resin (Millipore, A2220). Affinity-matrices were briefly washed twice with detergent buffer before elution of bound proteins in 10 µl 1xSDS-buffer without DTT. Aliquots of solubilisates and eluates were run on 10% or 12% SDS-PAGE and proteins transferred onto PVDF membranes. Immunodecorations were done with anti-HA (Thermo Scientific, #26183), anti-V5 (BioRad, #MCA1360) and anti-FLAG (Thermo Scientific, #MA1-91878) antibodies diluted 1:1000 in PBST + 3% BSA. Anti-HRP-conjugated secondary ABs (Abcam) in combination with ECL Prime (GE Healthcare) were used for visualization.

2D Blue Native/SDS-PAGE analysis of complexes

Protein complexes in mouse brain plasma membrane-enriched fractions (Kollewe et al., 2022; Schwenk et al., 2019; Schwenk et al., 2016) were solubilized with CL-47 (1 mg membrane protein / 1 ml CL-47 supplemented with 1 mM PMSF, 1 mM Iodoacetamide and a mixture of protease inhibitors (Leupeptin, Pepstatin A, Aprotinin). After clearing by ultracentrifugation (125,000xg, 10 min.) solubilisates were supplemented with 0.05% Coomassie® Brilliant Blue G-250 dye (Carl Roth) and 8% Glycerol. Protein complexes were separated on a 3-15% (w/v) acrylamide linear gradient gel (format 1.6 x 140 x 80 mm), made with 50 mM BisTris (pH 7,5), 50 mM α-capronicacid and 0,01% GDN (Anatrace, #GDN101). Solubilisates (1 ml) were loaded on 3 cm pockets and separated by electrophoresis (180 Volt, 32 mA, 45 min, 600 V, 6 hours) with 15 mM BisTris / 50 mM Tricine / 0.02% Coomassie G250 as cathode and 15 mM BisTris (pH 7.4) as anode buffer. Gel lanes were excised, cut in strips of 0.8 cm, incubated at 37°C for 20 min in 0.1% SDS (pH 8.8), 100 mM DTT and horizontally placed on top of 10% SDS-PAGE gels. After electrophoretic separation and transfer on a PVDF membrane proteins were stained with Ruby Blot stain to visualize abundant protein complexes, which were used as internal molecular weight standard for estimation of the apparent molecular sizes in the first dimension. PVDF membranes were cut horizontally at 50 kDa and 125 kDa. The low molecular weight section was immunodecorated with anti-T178B (LifeTein, #RB4235), the 50-125 kDa section with anti-PTPR (Neuromab, #75-194) and the high-molecular area with anti-NRX1-3 (LifeTein, #RB2987). Antibodies were diluted

1:1000 in PBST + 3% BSA. Anti-HRP-conjugated secondary ABs (Abcam) in combination with ECL Prime (GE Healthcare) were used for visualization.

ER complexome profiling

ER-enriched membrane fractions (Schwenk et al., 2019) were prepared from freshly isolated mouse brains and gently solubilized with CL-47 (salt replaced by 750 mM aminocaproic acid). After ultracentrifugation, 1 mg of solubilized protein was concentrated by ultracentrifugation into a 20%/50% sucrose cushion supplied with 0.125% Coomassie G250 Blue. The sample was then subjected to high-resolution cryo-slicing blue native gel mass spectrometry (csBN-MS) as described recently (Schulte et al., 2023). Briefly, the BN gel (1-18%) lane was sliced into 359 samples (0.3mm intervals), each digested with trypsin, and the obtained peptides (dissolved in 0.5% (v/v) trifluoroacetic acid) were measured on a QExactive mass spectrometer coupled to an UltiMate 3000 RSLCnano HPLC system (Thermo Scientific, Germany). After absorption on a C18 PepMap100 precolumn (300 µm i.d. × 5 mm; particle size 5 µm; 0.05% (v/v) trifluoroacetic acid; 5 min 20 µL/min), peptides were eluted with an aqueous-organic gradient (eluent A: 0.5% (v/v) acetic acid; eluent B: 0.5% (v/v) acetic acid in 80% (v/v) acetonitrile) as follows: 5 min 3% B, 120 min from 3% B to 30% B, 20 min from 30% B to 50% B, 10 min from 50% B to 99% B, 5 min 99% B, 5 min from 99% B to 3% B, 10 min 3% B (flow rate 300 nL/min). Separation column was a SilicaTip™ emitter (i.d. 75 µm; tip 8 µm; New Objective, USA) packed manually (23 cm) with ReproSil-Pur 120 ODS-3 (C18; particle size 3 µm; Dr. Maisch HPLC, Germany) from which eluting peptides were directly electrosprayed (2.3 kV; transfer capillary temperature 300°C) in positive ion mode. MS acquisition parameters were: maximum MS/MS injection time = 400 ms; dynamic exclusion duration = 60 s; minimum signal/intensity threshold = 40,000 (counts), top 15 precursors fragmented; isolation width = 1.4 m/z. Mass spectrometric raw data was processed as described above: mass offset-corrected peak lists were searched with 5 ppm mass tolerance against all mouse, rat, and human entries of the UniProtKB/Swiss-Prot database (release 20181205). Acetyl (Protein N-term), Carbamidomethyl (C), Gln->pyro-Glu (N-term Q), Glu->pyro-Glu (N-term E), Oxidation (M), Phospho (S, T, Y), and Propionamide (C) were chosen as variable modifications (fragment mass tolerance: 20 mmu), maximum one missed tryptic cleavage allowed; expect value cut-off for peptide assignment was set to 0.5. Proteins either representing exogenous contaminations (e.g., keratins, trypsin, IgG chains) or identified by only one specific peptide were not considered. Ion intensity information (peak volumes, PVs) extracted by MaxQuant and assigned to peptides after retention time-alignment of runs (RT tolerance 1 min, m/z tolerance 5 ppm) was used to compute protein abundance profiles as detailed in (Schulte et al., 2023). Slice numbers were converted to apparent molecular mass by fitting of log(MW) of marker complexes versus their observed peak maxima in abundance-mass profiles using a sigmoidal function. Abundance-mass profiles were finally smoothed using a gaussian filter (width set to 1.4).

Mass Spectrometry

Vacuum-dried peptides were dissolved in 13 µl or 20 µl of 0.5% (v/v) trifluoroacetic acid. Appropriate amounts were loaded onto trap columns (C18 PepMap100, 5 µm particles, Thermo Fisher Scientific GmbH, Dreieich, Germany) with 0.05% trifluoroacetic acid and separated on C18 reversed phase columns (SilicaTip emitters, 75 µm i.d., 8 µm tip, New Objective, Inc, Littleton, USA, manually packed 11 to 12 cm (Orbitrap Elite mass spectrometer) or 21 to 22 cm (QExactive HF-X mass spectrometer) with ReproSil-Pur ODS-3, 3 µm particles, Dr. A. Maisch HPLC GmbH, Ammerbuch-Entringen, Germany; flow rate: 300 nL/min) using UltiMate 3000 RSLCnano HPLC systems (Thermo Fisher Scientific GmbH, Dreieich, Germany). Gradients were built with eluent ˈAˈ (0.5% (v/v) acetic acid in water) and eluent ˈBˈ (0.5% (v/v) acetic acid in 80% (v/v) acetonitrile / 20% (v/v) water): 5 min 3% ˈBˈ, 60 min from 3% ˈBˈ to 30% ˈBˈ, 15 min from 30% ˈBˈ to 99% ˈBˈ, 5 min 99% ˈBˈ, 5 min from 99% ˈBˈ to 3% ˈBˈ, 15 min 3% ˈBˈ (Orbitrap Elite mass spectrometer) or up to 5 min 3% ˈBˈ, 120 min from 3% ˈBˈ to 30% ˈBˈ, 20 min from 30% ˈBˈ to 40% ˈBˈ, 10 min from 40% ˈBˈ to 50% ˈBˈ, 5 min from 50% ˈBˈ to 99% ˈBˈ, 5 min 99% ˈBˈ, 5 min from 99% ˈBˈ to 3% ˈBˈ, 10 min 3% ˈBˈ (QExactive HF-X mass spectrometer). Eluting peptides were electro-sprayed at 2.3 kV (positive polarity) via Nanospray Flex ion sources into an Orbitrap Elite mass spectrometer (CID fragmentation of the 10 most abundant at least doubly charged new precursors per scan cycle) or into a QExactive HF-X mass spectrometer (HCD fragmentation of the 25 most abundant doubly, triply, or quadruply charged new precursors per scan cycle; Figs. 1B, 3B) (all Thermo Fisher Scientific GmbH, Dreieich, Germany) and analyzed with the following major settings: scan range 370 to 1,700 m/z, full MS resolution 240,000, dd-MS2 resolution ˈnormalˈ (ion trap) or 15,000, respectively, maximum dd-MS2 injection time 200 ms or 100 ms, respectively, intensity threshold 2,000 or 40,000, respectively, dynamic exclusion 30 s or 60 s, respectively, isolation width 1.0 m/z. LC-MS/MS RAW files were converted into peak lists (Mascot generic format, mgf) with ProteoWizard msConvert (https://proteowizard.sourceforge.io/). All peak lists were searched twice with Mascot Server 2.6.2 (Matrix Science Ltd, London, UK) against a database containing all mouse, rat, and human entries of the UniProtKB/Swiss-Prot database. Initially broad mass tolerances were used. Based on the search results peak lists were linear shift mass recalibrated using in-house developed software and searched again with narrow mass tolerances for high-resolution peaks (peptide mass tolerance ± 5 ppm; fragment mass tolerance 0.8 Da for Orbitrap Elite peak lists and ± 20 mmu for Q Exactive HF-X peak lists). One missed trypsin cleavage and common variable modifications were accepted. Default significance threshold ($p < 0.05$) and an expect value cut-off of 0.5 were used for displaying search results.

MS quantification of proteins

Proteins were evaluated by a label-free quantification procedure (Kocylowski et al., 2022). MaxQuant v1.6.3 (http://www.maxquant.org) was used for mass calibration and to extract from FT full scans peptide signal intensities (peak volumes, PVs). The

elution times of peptide PVs were aligned (pairwise, Loess regression) and assigned to peptides by matching m/z and elution times acquired by MS/MS identification (tolerances 2-3 ppm / ± 1 min) as described (Bildl et al., 2012). The obtained PV tables (protein-specific peptide signal intensities in all runs) were then further processed to eliminate the influence of PV outliers, false assignments and gaps by exploring the consistency of PV relations within proteins (i.e. protein-specific PV ratios between and within runs). Orthogonal combinations of these relations provided 'expected PV values' (EPVs) for each interconnected PV value that served as a measure of accuracy and weighting factor. In addition, time- and run-dependent detectability thresholds were estimated for each cell in the PV table based on the distribution of measured PVs (3rd percentile within a 3 min elution time window). Qualified PV data in each protein PV matrix was then aggregated to obtain global protein references termed 'protein reference ridges' (i.e. vectors that represent the maximum protein coverage of MS/MS-identified and quantified peptides with their ionization efficiencies). In a final step, proteins were quantified by weighted fitting of their measured peptide PVs to their respective reference ridge. In case no (consistent) peptide PVs were identified, an apparent protein detection limit was determined using the detectability thresholds of the three best ionizing peptides fitted to the protein reference ridge. $Abundance_{norm}spec$ values (as a measure of molecular abundance) were calculated as described (Bildl et al., 2012) from the fitted protein ridges. This procedure is comparable to MaxQuant LFQ ((Cox et al., 2014); all data is fitted without weighting), but quantification is more robust and accurate, in particular for sparse PV data.

Determination of specificity in APs was based on target-normalized abundance ratios (tnRs) of proteins in target APs versus control APs (calculated as described in (Kocylowski et al., 2022)) together with information on molecular abundance and detection thresholds of proteins. These information were collectively inspected using the BELKI software suite (https://github.com/phys2/belki). For large data sets tnR-values were visualized by t-distributed stochastic neighbour embedding (t-SNE, with perplexity of 50, Figures 1C, 4); comparison of two APs was illustrated as 2D-scatter plot of tnR-values (Figure 2B). Specific co-purification was defined by two criteria: First, tnR values of ≥ 0.25 were set as specificity-threshold (Kocylowski et al., 2022), unless high-quality ABs or stringent negative controls (target knock-out) allowed reduce of the threshold to 0.2. Second, consistency (of specific co-purification) among APs was applied (Table 1, S1-4, Figure 5), i.e. co-purification of a given protein was dubbed specific, if its tnR-value(s) exceeded the specificity-threshold in APs with more than two (or the majority of) target ABs or in replicate experiments. Details about the experiments (ABs, controls), tnR-pairs and specificity-thresholds for each experimental series are indicated in Tables S1-4. Calculations of protein abundance ratios used to determine the degree of association of co-purified proteins relative to the target NRX1A (Figure 1D) were based on $abundance_{norm}spec$ values. Similarly, $abundance_{norm}spec$ values were used to judge the impact of GPI-modification in NRX3A on protein-protein interactions (Figure 2C), to reveal changes on NRX1-3 complexes by enzymatic removal of HS-moieties (Figure 2D), and to

monitor alterations in NRX1-3/PTPRS complex formation after sh-RNA mediated knockdown of T178B (Figure 3C). For direct comparison, data sets were normalized to target values and thus providing average fluctuations in association with specific target proteins. For evaluation of whole membrane fractions from neuronal cultures treated with AAVs for sh-178B or control AAVs, total protein amounts were equilibrated to correct for systematic deviations due to technical variations (e.g. sample loading, in-gel digest etc.); normalization factors were smaller than 1.3. All these experiments were done in triplicates and values are given as mean ± SEM.

For UMAP-analysis of the NRX-T178-PTPR associated networks (Figure S8), $abundance_{norm}Spec$ values of 172 proteins, identified as specific interactors in target APs (30 targets outlined in Figure 5 (except of GRIA) and replicate experiments, indicated in Tables S1-S4), were used to uncover data structures pointing towards clusters or preferred assemblies. The UMAP (Sainburg et al., 2021) method was used to reduce the dimensionality of the normalized data, leveraging the software provided by McInnes *et al.* (https://doi.org/10.21105/joss.00861), which is based in the programming language Python (Van Rossum and Drake Jr, 1995). The Euclidean distance was chosen as the metric for clustering the data. The parameter constraining the size of the local neighborhood of a data instance (n_neighbors) was 10. Additionally, the Python library pandas (10.5281/zenodo.3509134) was used for data handling. Visualization of reduced data was done using the Bokeh library (http://www.bokeh.pydata.org.)

Neuronal culture and sh-mediated knockdown

Brains were dissected from P18 rat embryos. Hippocampi and cortices of both hemispheres were dissected and transferred into HBSS buffer. Tissue pieces were trypsinized and briefly washed with HBSS buffer after stopping the enzymatic treatment by adding FCS. Cells were dissociated by trituration with a fire polished Pasteur pipettes. Vital cells were plated at high density (500,000 cells/well) for biochemical experiments or medium density (50,000 cells/well) for immunofluorescence experiments on poly-D-Lysine coated wells. For immunostainings cells were cultivated on coated glass coverslips. Neurobasal medium conditioned by cultivated glia cells was added at the start of the culture and freshly every week. Growing of mitotic cells was blocked by supplementing the medium with 5 µM AraC.

Knockdown of T178B by sh-T178B was induced by adding AAV DJ8 particles carrying sequences for H1 promoter-regulated transcription of sh-T178B (sh#1: GCCAGGAAGCACAGGGACA; sh#2: ACTTTGAGCTATCACGTTA) and GFP, whose expression is controlled by an ubiquitin promoter. Control viruses were driving sole GFP expression. Successful infection and vitality of cultured neurons were controlled regularly; cultures were maintained 2.5 up to 3 weeks to ensure synapse maturation and a quantitative elimination of T178B. Neurons were then used either for immunostainings or biochemical experiments. For the latter, neurons were released by cell scrapers and homogenized in 10 mM HEPES, 320 mM sucrose (pH 7.4) and protease inhibitors by up and down pipetting. After

ultracentrifugation (125,000xg, 20 min.) the cell pellets were homogenized in 20 mM Tris/HCl (pH 7.4) and protein concentrations were determined by Bradford. Equal amounts of proteins (control, sh-treated neurons) were denatured by adding 10 µl Laemmli-buffer, separated on SDS-PAGE and silver stained. Bands were cut in low and high molecular weight pieces and subjected to tryptic digest for nano-LC MS/MS (Figure 3B, Table S3). For analysis (Figure 3C) of protein assemblies, neurons were solubilized in CL-91 buffer and NRX and PTPRS complexes were affinity-isolated and processed for MS-analysis as described above. In addition, small aliquots of solubilisates and eluates were run on 10% SDS-PAGE and proteins transferred onto PVDF membranes. Blots were cut at 50 and 125 kDa and then separately immunodecorated with anti-T178B (LifeTein, #RB4235), anti-PTPR (Neuromab, #75-194) and anti-NRX1 (Millipore, ABN161-I). Antibodies were diluted 1:1000 in PBST + 3% BSA. Anti-HRP-conjugated secondary antibodies (Abcam) in combination with ECL Prime (GE Healthcare) were used for visualization.

Immunofluorescence

Neurons seeded on coverslips were selected between DIV 14-21. For total stains, neurons were washed with PBS, permeabilized by adding PBS containing 1% BSA and 0.05% Triton ™ X-100 for 30 min, transferred on a linear plate and incubated for 1 h with primary ABs (PTPRS, #AF3430; MAP2, Abcam, #ab5392, dilution 1:100) PBS containing 1% BSA. After two rounds of washing steps with PBS, secondary ABs conjugated with selected fluorophores Alexa 555 or Alexa647 diluted (1:1000) were added. Neurons were incubated for 30 min in a covered plate and, after short washing with PBS and water, mounted with FluorSave™ Reagent (Millipore, 345789-20ML) on microscope slides (Carl-Roth, H883). After drying overnight, mounted neurons were stored at 4°C until further analysis. For surface staining, culture media was removed and exchanged with 100 µl filtered PBS. 2 µl of selected primary ABs were added, followed by an incubation period for 30 min on ice to avoid AB-internalization. Neurons were fixed with 4% PFA in PBS for 10 min at RT. Subsequently, they were washed twice with 1 ml filtered PBS and blocked with PBS containing 1% BSA for 30 min. The remaining procedure was kept as described for permeabilized neurons.

Evaluation and quantification of immunostainings

Immunolabeled cells were explored with a LSM 710 Meta confocal microscope (Zeiss). Single planes of z-stack series of digital images taken at different z-planes were acquired with a 63x/1.4 Oil DIC objective (Zeiss). Digital images were captured using ZEN (Black Edition) Software (Zeiss Microscopy, Germany). Two-dimensional maximum intensity projections were generated by Fiji (open source SciJava software ecosystem) (Schindelin et al., 2012). Images were exported and quantitative analysis was performed with Fiji. Regions of interest (ROIs) in the dendrites of infected and control neurons were selected and examined (n= 12-15 neurons, 3 dendritic ROIs per neuron). PTPRS was used for staining together with MAP2 and GFP serving as volumetric markers to define quantification areas in

dendrites. Analysis was performed both in permeabilized neurons (to calculate total protein amount) and in non-permeabilised neurons to quantify the surface levels of PTPRS. Data on dendritic intensity are given as mean ± SEM, significance of differences was assessed by unpaired Student's t test.

Transcript expression pattern

Transcript levels of individual genes in defined cell-types were calculated using the online software DropViz (Saunders et al., 2018). For this purpose, all subclusters assigned to a particular cell-type, according to the common name function of DropViz, were combined to a meta-group using the cluster comparison feature of DropViz with default parameter settings. The RNA count of a selected gene per 100,000 unique molecular identifiers in the meta-group was then given as target sum per 100k in a downloadable table containing differentially expressed genes.

Electrophysiology

In Vivo Stereotactic Injection

The distinct AAVs were injected into C57BL/6 mice 20–23 days after birth (P20-P23). Animals were anesthetized by injection of a ketamine/dorbene mixture and mounted in a Kopf stereotaxic frame (Tujunga). Virus-containing solution (0.5–1 µl) was injected at a single site into the hippocampus (targeting the CA3 region) by means of a UMP3 controller (WPI, Sarasota) and a nanofil syringe/needle (WPI, Sarasota). Following surgery, pups recovered rapidly by antagonist injection and were returned to their home cage. Recordings were performed 4-5 weeks following virus injection. Animal procedures were in accordance with national and institutional guidelines and approved by the Animal Care Committee Freiburg according to the Tierschutzgesetz (AZ G-21/40).

Slice preparation

Transverse 300-µm-thick hippocampal slices were cut from brains of 1- to 2-month-old WT mice, as described (Boudkkazi et al., 2014). Hippocampal slices were cut in ice-cold, sucrose-containing physiological saline using a commercial vibratome (VT1200S, Leica Microsystems). Slices were incubated at 35°C, transferred into a recording chamber, and super-fused with physiological saline at room temperature.

Patch-clamp recordings in brain slices

Patch pipettes were pulled from borosilicate glass (Hilgenberg; outer diameter, 2 mm; wall thickness, 0.5 mm for somatic recordings). When filled with internal solution, they had resistances of ~2–4 MΩ postsynaptic pipettes. Patch pipettes were positioned using Kleindiek micromanipulator (Kleindiek Nanotechnik, Reutlingen). A Multiclamp 700B amplifier (Molecular Devices, Sunnydale) was used for recordings. Pipette capacitance of both electrodes was compensated to 70%-90%. Voltage and current signals were filtered at 10 kHz with the built-in low-pass Bessel filter and digitized at 20 kHz using a Digidata 1440A (Molecular Devices, Sunnydale). pClamp10 software (Molecular Devices, Sunnydale) was used for

stimulation and data acquisition. Holding potential of CA1 pyramidal neuronal was -70 mV (to record AMPAR-mediated EPSCs). Synaptic responses were evoked by stimulation at 0.1 Hz with a monopolar glass electrode filled with ACSF in the stratum radiatum of CA1 for CA1 pyramidal neurons. To ensure stable recording, membrane holding current, input resistance, and pipette series resistance were monitored throughout the recording.

Solutions

For dissection and storage of slices, a sucrose-containing physiological saline containing 87 mM NaCl, 25 mM $NaHCO_3$, 25 mM D-glucose, 75 mM sucrose, 2.5 mM KCl, 1.25 mM NaH_2PO_4, 0.5 mM $CaCl_2$, and 7 mM $MgCl_2$ was used. Slices were superfused with physiological extracellular solution that contained 125 mM NaCl, 25 mM $NaHCO_3$, 2.5 mM KCl, 1.25 mM NaH_2PO_4, 1 mM $MgCl_2$, 2 mM $CaCl_2$, and 25 mM glucose (equilibrated with a 95% O_2/5% CO_2 gas mixture). Pipettes were filled with a K-methylsulfonate intracellular solution containing 120 mM $KMeHSO_3$, 20 mM KCl, 2 mM $MgCl_2$, 2 mM Na_2ATP, 10 mM HEPES, and 0.1 mM EGTA. Membrane potentials are given without correction for liquid junction potentials. Values given throughout the manuscript indicate mean ± SEM or SD. Significance of differences was assessed by a nonparametric Mann-Whitney test.

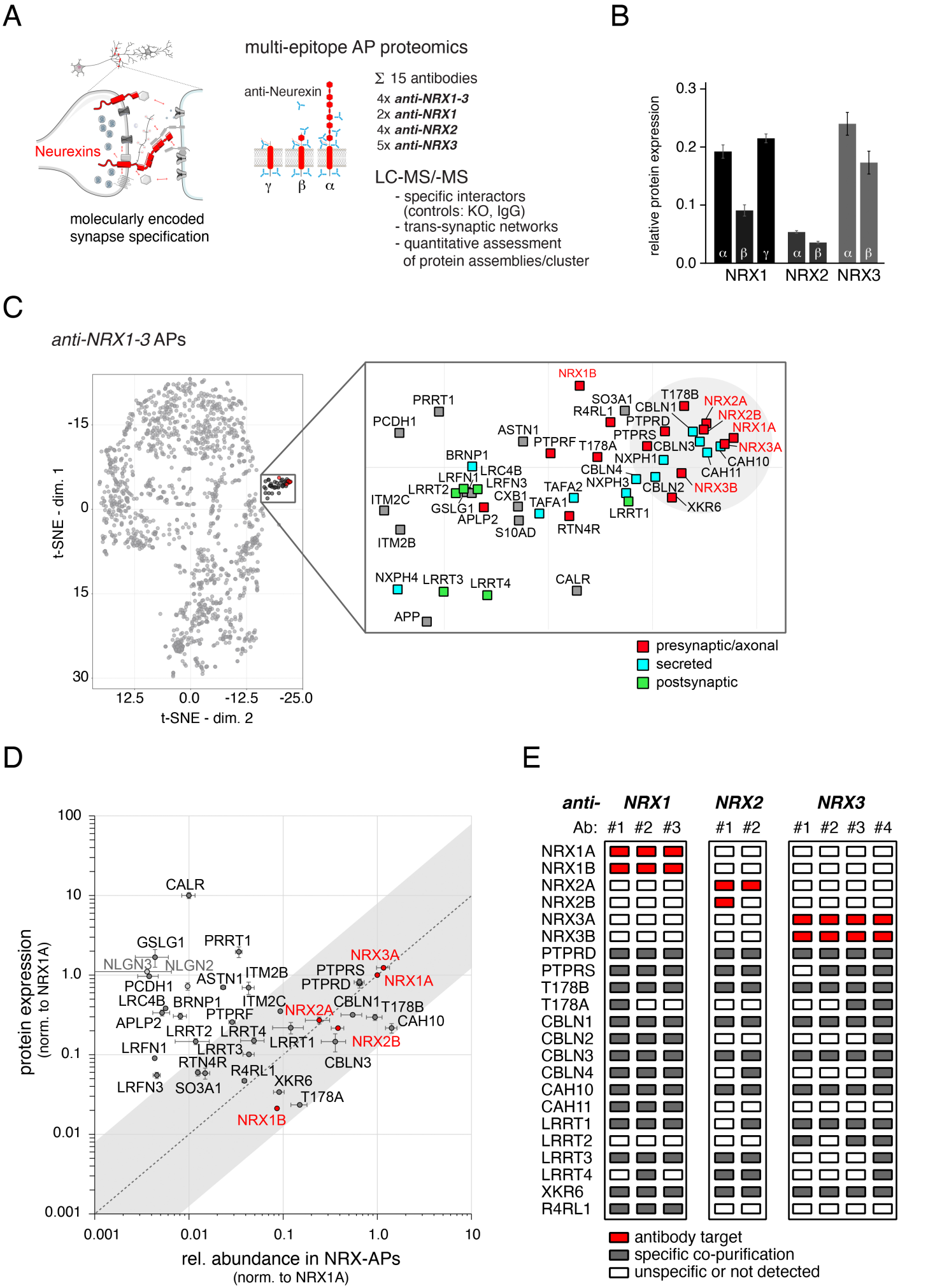

Figure 1, Thivaios et al.

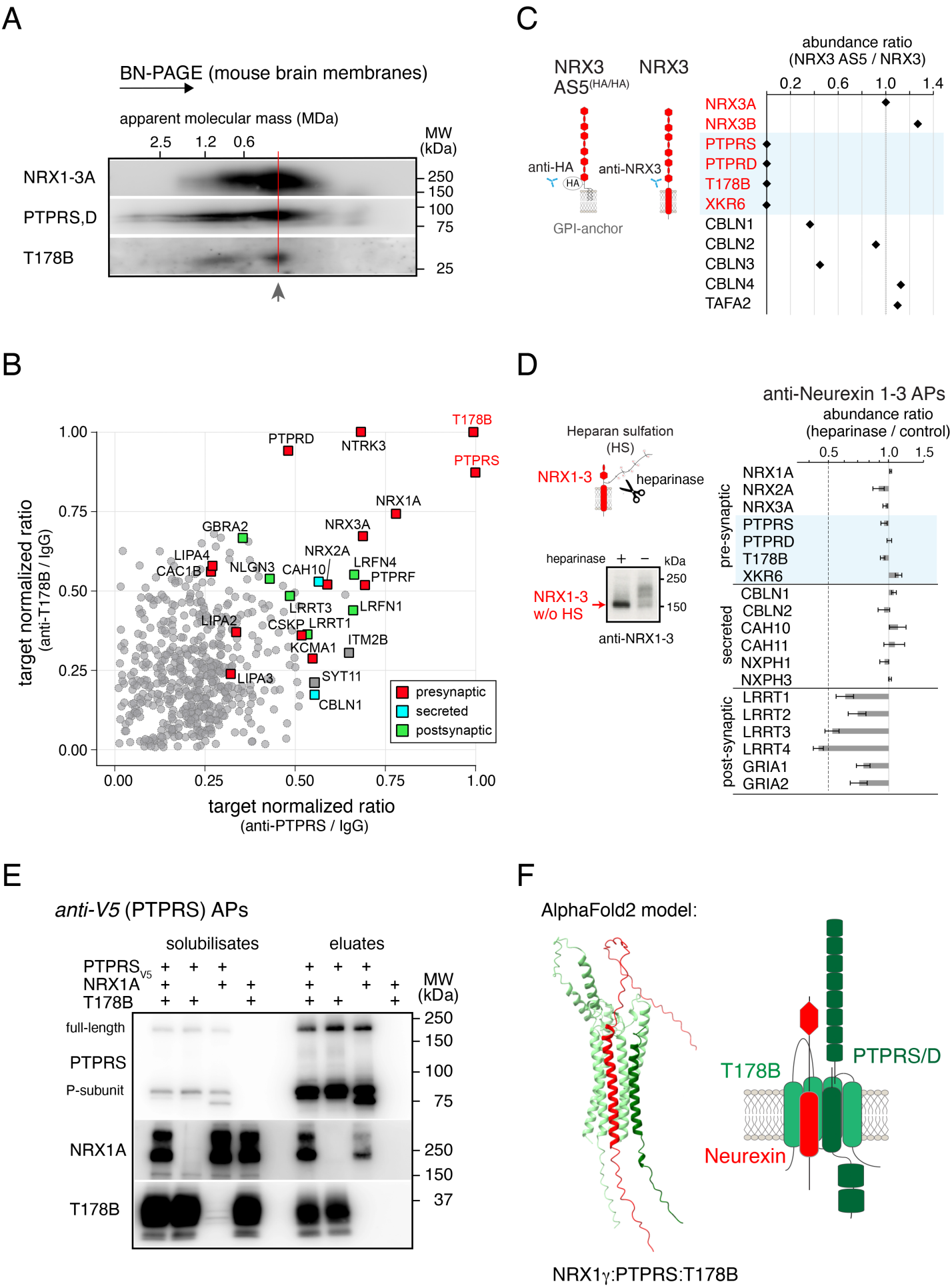

Figure 2, Thivaios et al.

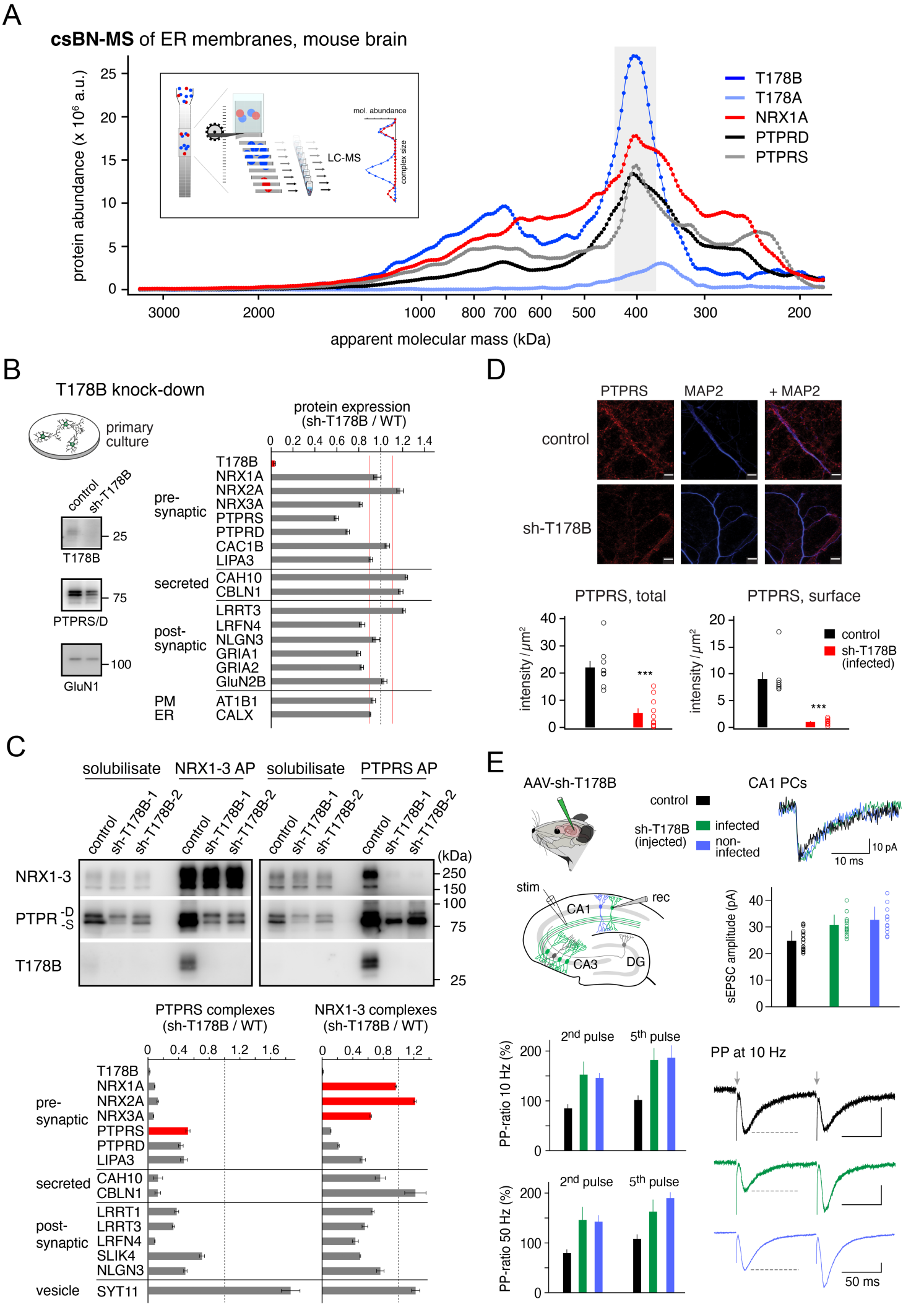

Figure 3, Thivaios et al.

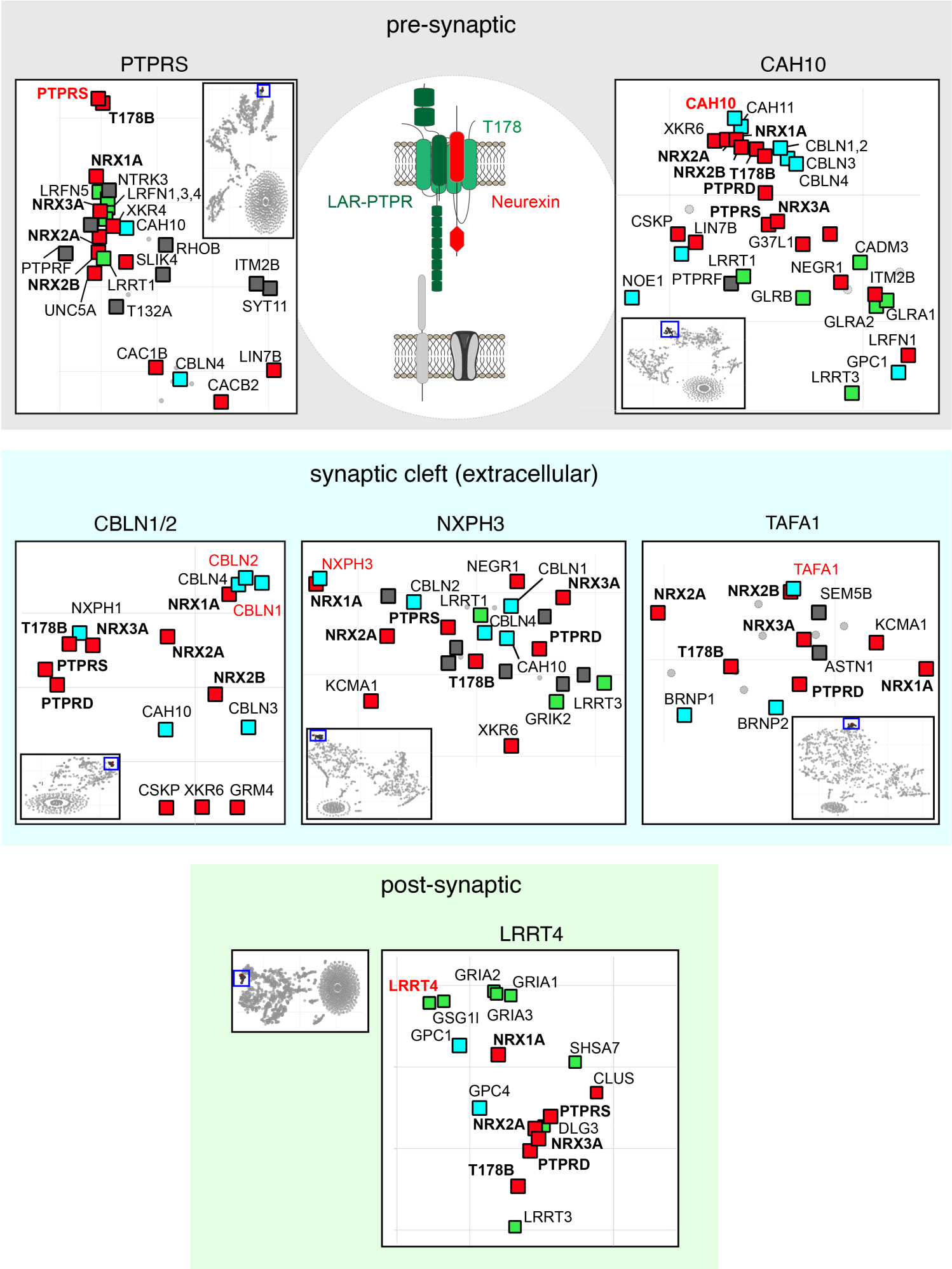

Figure 4, Thivaios et al.

Synaptic connectome associated with NRX-T178-PTPRs

30 targets (for meAP-MS)

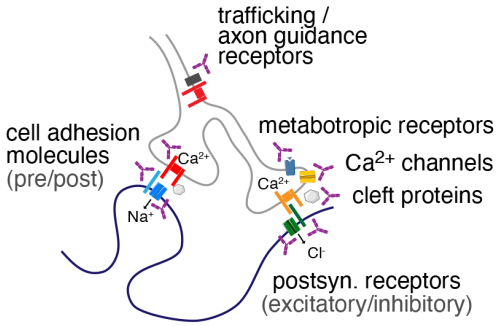

name	Synonym/description	name	Synonym/description
Presynaptic NRX-T178-rPTP module		**Secreted/extracellular/synaptic cleft**	
NRX1/2/3	Neurexins	CBLN1/2	Cerebellin 1/2
PTPRS/D	LAR-RPTPs	CAH10	CA10, Carbonic anhydrase-rel.
T178B	Transmembrane protein 178B	TAFA1/2	FAM19A1/2
Cell adhesion molecules (CAMs)		NXPH1/3	Neurexophilin 1/3
LRRT1-4	LRRTMs	**Ion channels and receptors**	
NLGN1/2/3	Neuroligins	Cav2	Ca^{2+} channels
Axon guidance, trafficking		GRIA	AMPA-type glutamate receptor
APP	Amyloid-b precursor protein	GBRA/G	GABA(A) receptor
APLP2	Amyloid-b prec. like protein 2	GRM4	mGluR4
SYT11	Synaptotagmin 11	**Unknown**	
RTN4R	Nogo receptor	XKR6	XK-related protein 6

synaptic NRX-T178-PTPR connectome

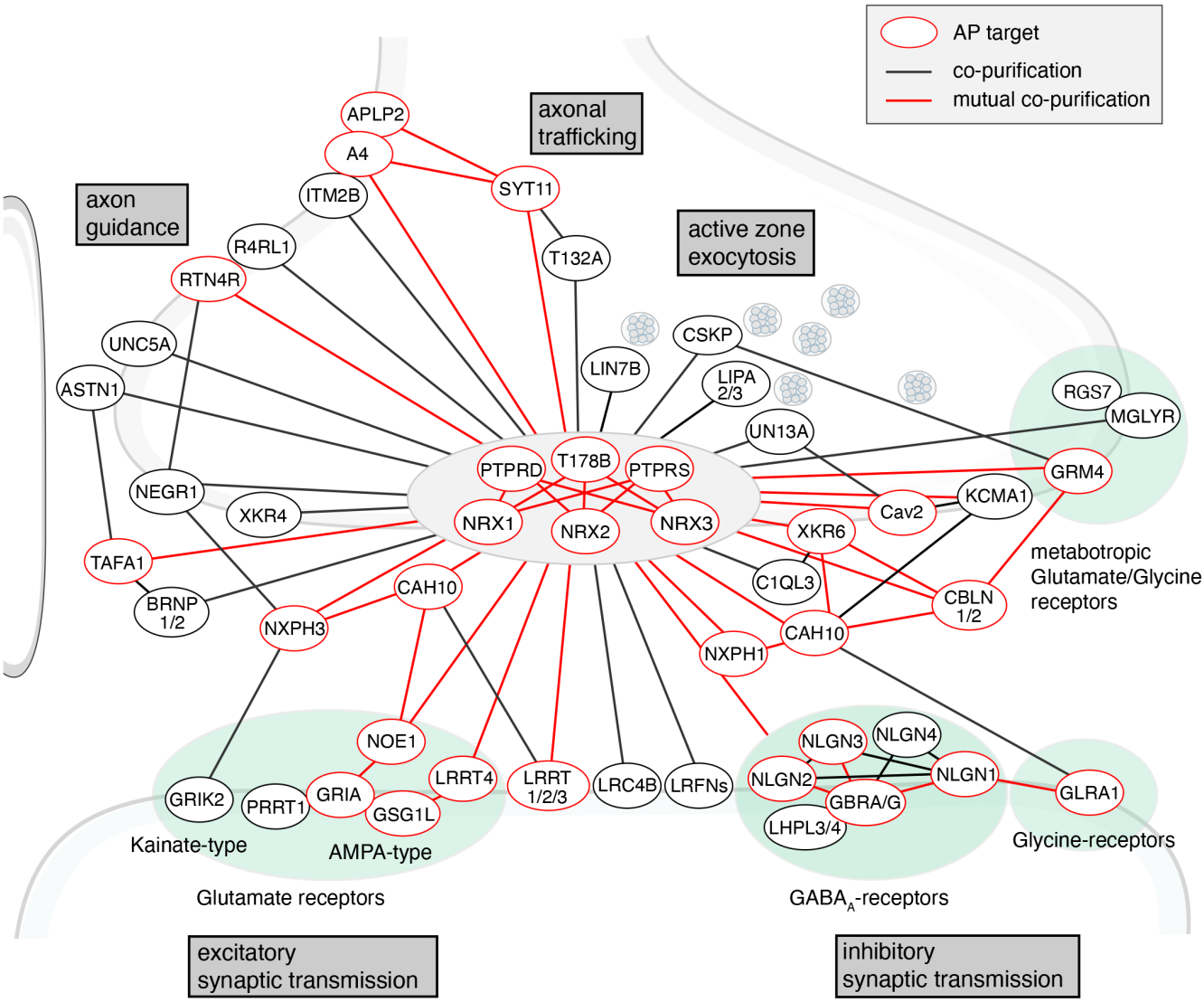

Figure 5, Thivaios et al.

Table 1 – Proteins specifically co-purified with anti-Nrx1-3 antibodies

Protein ID	Gene name	Acc.No.	Description	Mass (kDa)	Function	Refs.
NRX1A	*Nrxn1*	Q9CS84	Neurexin-1-alpha	166	synaptic organizer	(1)
NRX1B	*Nrxn1*	P0DI97	Neurexin-1-beta	50	synaptic organizer	(1)
NRX1G	*Nrxn1*	Q9CS84-6	Neurexin-1-gamma	15	synaptic organizer	(2)
NRX2A	*Nrxn2*	E9Q7X7	Neurexin-2-alpha	185	synaptic organizer	(1)
NRX2B	*Nrxn2*	E9PUN2	Neurexin-2-beta	70	synaptic organizer	(1)
NRX3A	*Nrxn3*	Q6P9K9	Neurexin-3-alpha	173	synaptic organizer	(1)
NRX3B	*Nrxn3*	Q8C985	Neurexin-3-beta	62	synaptic organizer	(1)
A4	*App*	P12023	Amyloid-beta precursor protein, A4 protein	87	axon growth	(3)
***AGRB1**	*Adgrb1*	Q3UHD1	Adhesion GPCR B1	173	adhesion GPCR	(4)
***APLP2**	*Aplp2*	Q06335	Amyloid beta precursor like protein 2	80	axon growth	(3)
***ASTN1**	*Astn1*	Q61137	Astrotactin-1	145	surface receptor	(5)
***ASTRB**	*Gramd1b*	Q80TI0	Protein Aster-B	85	transporter	(6)
***BRNP1**	*Brinp1*	Q920P3	BMP/retinoic acid-inducible neural-specific protein 1	89	neuronal development	(7)
***BRNP2**	*Brinp2*	Q6DFY8	BMP/retinoic acid-inducible neural-specific protein 2	89	neuronal development	(7)
C1QL3	*C1ql3*	Q9ESN4	Complement C1q-like protein 3	27	synaptic organizer	(8)
***CADM3**	*Cadm3*	Q99N28	Cell adhesion molecule 3	43	cell adhesion	(9)
CAH10	*Ca10*	P61215	Carbonic anhydrase-related protein 10	38	cell adhesion	(2)
CAH11	*Ca11*	O70354	Carbonic anhydrase-related protein 11	36	cell adhesion	(2)
CALR	*Calr*	P14211	Calreticulin	48	protein folding	(10)
CBLN1	*Cbln1*	Q9R171	Cerebellin-1	21	synaptic organizer	(11)
CBLN2	*Cbln2*	Q8BGU2	Cerebellin-2	24	synaptic organizer	(12)
CBLN3	*Cbln3*	Q9JHG0	Cerebellin-3	21	synaptic organizer	(12)
CBLN4	*Cbln4*	Q8BME9	Cerebellin-4	22	synaptic organizer	(12)
***CLUS**	*Clu*	Q06890	Clusterin	52	cell adhesion	(13)
***CNTN1**	*Cntn1*	P12960	Contactin-1	113	cell adhesion	(14)
***GRIA1**	*Gria1*	P23818	Glutamate (AMPA-type) receptor 1, GluA1	102	ion channel	(15)
***GRIA2**	*Gria2*	P23819	Glutamate (AMPA-type) receptor 2, GluA2	99	ion channel	(15)
***GRIA3**	*Gria3*	Q9Z2W9	Glutamate (AMPA-type) receptor 3, GluA3	101	ion channel	(15)
***GRM4**	*Grm4*	Q68EF4	Metabotropic glutamate receptor 4, mGluR4	101	GPCR	(16)
***GSLG1**	*Glg1*	Q61543	Golgi apparatus protein 1	134	cell adhesion	(17)
***ITM2B**	*Itm2b*	O89051	Integral membrane protein 2B	30	unknown (modulator of APP processing)	(18)
***ITM2C**	*Itm2c*	Q91VK4	Integral membrane protein 2C	30	unknown (modulator of APP processing)	(19)
***KCJ10**	*Kcnj10*	Q9JM63	Inward rectifier K^+ channel 10, Kir4.1	43	ion channel	(20)
***KCMA1**	*Kcnma1*	Q08460	Ca^{2+}-activated K^+ channel; BK_{Ca}	134	ion channel	(21)
***LRC4B**	*Lrrc4b*	P0C192	Leucine-rich repeat-containing protein 4B	76	cell adhesion	(22)
***LRFN1**	*Lrfn1*	Q2WF71	Leucine-rich repeat and fibronectin type III domain-containing protein 1	82	cell adhesion	(23)
***LRFN3**	*Lrfn3*	Q8BLY3	Leucine-rich repeat and fibronectin type-III domain-containing protein 3	66	cell adhesion	(23)

LRRT1	*Lrrtm1*	Q8K377	Leucine-rich repeat transmembrane neuronal protein 1	59	cell adhesion	(24)
LRRT2	*Lrrtm2*	Q8BGA3	Leucine-rich repeat transmembrane neuronal protein 2	59	cell adhesion	(24)
LRRT3	*Lrrtm3*	Q8BZ81	Leucine-rich repeat transmembrane neuronal protein 3	66	cell adhesion	(25)
LRRT4	*Lrrtm4*	Q80XG9	Leucine-rich repeat transmembrane neuronal protein 4	67	cell adhesion	(26)
***MGLYR**	*Gpr158*	Q8C419	Metabotropic glycine receptor, mGlyR, GPCR 158	134	GPCR	(27)
NLGN1	*Nlgn1*	Q99K10	Neuroligin-1	94	cell adhesion	(28)
NLGN2	*Nlgn2*	Q69ZK9	Neuroligin-2	91	cell adhesion	(28)
NLGN3	*Nlgn3*	Q8BYM5	Neuroligin-3	91	cell adhesion	(28)
***NSG2**	*Nsg2*	P47759	Neuronal vesicle trafficking-associated protein 2	19	vesicle transport	(29)
NXPH1	*Nxph1*	Q61200	Neurexophilin-1	31	cell adhesion	(30)
NXPH3	*Nxph3*	Q91VX5	Neurexophilin-3	28	cell adhesion	(30)
NXPH4	*NXPH4*	O95158	Neurexophilin-4	33	cell adhesion	(30)
***PCDH1**	*PCDH1*	Q08174	Protocadherin-1	115	axon growth	(31)
***PRRT1**	*Prrt1*	O35449	Proline-rich transmembrane protein 1	31	synaptic plasticity	(32)
PTPRD	*Ptprd*	Q64487	Receptor-type tyrosine-protein phosphatase D	214	synaptic organizer	(33)
PTPRF	*Ptprf*	A2A8L5	Receptor-type tyrosine-protein phosphatase F	211	synaptic organizer	(33)
PTPRS	*Ptprs*	B0V2N1	Receptor-type tyrosine-protein phosphatase S	212	synaptic organizer	(33)
***R4RL1**	*Rtn4rl1*	Q8K0S5	Reticulon-4 receptor-like 1	50	axon guidance	(34)
***RGS7**	*Rgs7*	O54829	Regulator of G-protein signaling 7	55	GPCR	(27)
***RTN4R**	*Rtn4r*	Q99PI8	Reticulon-4 receptor, NoGo-receptor	51	axon guidance	(34)
***SLIT1**	*Slit1*	Q80TR4	Slit homolog 1 protein	167	axon guidance	(35)
***SLIT2**	*Slit2*	Q9R1B9	Slit homolog 2 protein	169	axon guidance	(35)
***SLIT3**	*Slit3*	Q9WVB4	Slit homolog 3 protein	168	axon guidance	(35)
***SO3A1**	*Slco3a1*	Q8R3L5	Solute carrier organic anion transporter family member 3A1	77	transporter	(36)
SYT11	*Syt11*	Q9R0N3	Synaptotagmin-11	48	vesicle protein	(37)
***T132A**	*Tmem132a*	Q922P8	Transmembrane protein 132A	110	unknown	(38)
***T178A**	*Tmem178a*	Q9CZ16	Transmembrane protein 178A	33	unknown	
***T178B**	*Tmem178b*	H3BS89	Transmembrane protein 178B	33	unknown	
TAFA1	*Tafa1*	Q7TPG8	Chemokine-like protein TAFA-1, FAM19A	15	cell adhesion	(39)
TAFA2	*Tafa2*	Q7TPG7	Chemokine-like protein TAFA-2, FAM19B	15	cell adhesion	(39)
***TRPV2**	*Trpv2*	Q9WTR1	Transient receptor potential channel TRPV2	86	ion channel	(40)
***VWA8**	*Vwa8*	Q8CC88	von Willebrand factor A domain-containing protein 8	213	unknown	
***XKR4**	*Xkr4*	Q5GH67	XK-related protein 4	72	scramblase	(41)
***XKR6**	*Xkr6*	E9Q6C8	XK-related protein 6	71	unknown	

* proteins not previously related to NRX

References

1. Südhof TC. Cell. 2017;171(4):745–69.
2. Sterky FH et al. Proc Natl Acad Sci U S A. 2017;114(7):E1253–62.
3. Aydin D et al. Exp brain Res. 2012;217(3–4):423–34.
4. Wang J et al. Cell. 2021;184(24):5869-5885.e25.
5. Fishell G et al. Development 1991; 113(3):755–65.
6. Sandhu J et al. Cell 2018 ;175(2):514-529.e20.
7. Terashima M et al. J Neurosci Res 2010;88(7):1387–93.
8. Matsuda K et al. Neuron 2016;90(4):752–67.
9. Frei JA, Stoeckli ET. Mol Cell Neurosci. 2017;81:41–8.
10. Michalak M. J Cell Mol Med. 2024;28(5).
11. Uemura T et al. Cell 2010;141(6):1068–79.
12. Südhof TC. Curr Opin Neurobiol. 2023 Aug 1;81
13. Silkensen JR et al. J Clin Invest 1995;96(6):2646.
14. Dityatev A et al. Neuron Glia Biol 2008;4(3):197–209.
15. Cull-Candy S et al. Curr Opin Neurobiol 2006;16(3):288–97.
16. Ramos C et al. J Biol Chem. 2012;287(24):20176–86.
17. Steegmaler M et al. Nature;373(6515):615–20.
18. Matsuda S et al. J Biol Chem. 2005;280(32):28912–6.
19. Dinamarca MC et al. Nat Commun. 2019;10(1).
20. Nwaobi SE et al. Acta Neuropathol 2016;132(1).
21. Griguoli M et al. J Physiol. 2016;594(13):3489–500.
22. Woo J et al. Nat Neurosci. 2009 Apr;12(4):428–37.
23. Lie E et al. Front Mol Neurosci 2018;11:105.
24. Soler-Llavina GJ et al. Neuron 2013;79(3):439–46.
25. Um JW et al. Cell Rep 2016;14(4):808–22.
26. DeWit J et al. Neuron 2013;79(4):696–711.
27. Laboute T et al. Science 2023;379(6639):1352–8.
28. Varoqueaux F et al. Neuron 2006;51(6):741–54.
29. Debaigt C et al. J Biol Chem 2004;279(34):35687–91.
30. Missler M et al. J Biol Chem 1998;273(52):34716–23.
31. Lu WC et al. Neural Regen Res 2018;13(3):427–33.
32. Matt L et al. Cell Rep. 2018;22(9):2246–53.
33. Cornejo Fet al. Front cell Dev Biol 2021;9.
34. Yoo SW et al. J Comp Neurol 2017;525(2):291–301.
35. Nguyen-Ba-Charvet KT, Chédotal A. J Physiol Paris 2002;96(1–2):91–8.
36. Pan Q et al. Gastroenterology 2018;155(5):1578-1592.e16.
37. Trovo L et al EMBO Rep 2024 (in press)
38. Li B et al. Development 2022;149(17).
39. Khalaj AJ et al. J Cell Biol. 2020;219(9).
40. Kojima I, Nagasawa M. Handb Exp Pharmacol 2014;222:247–72.
41. Suzuki J et al. J Biol Chem 2014;289(44):30257–67.

Supplemental Information

A ternary Neurexin-T178-PTPR complex represents a core-module of neuronal synapse organization

Spyros Thivaios, Jochen Schwenk, Aline Brechet, Sami Boudkkazi, Phil Henneken, Maciej K. Kocylowski, Alexander Haupt, Debora Kaminski, Jean-Baptiste van den Broucke, Dietmar Schreiner, Uwe Schulte, Fredrik H. Sterky, Michisuke Yuzaki, Peter Scheiffele, Bernd Fakler

Inventory

Supplementary Figures

- Figure S1 (related to Figure 1)
- Figure S2 (related to Figure 1)
- Figure S3 (related to Figures 1-5)
- Figure S4 (related to Figure 1)
- Figure S5 (related to Figure 1)
- Figure S6 (related to Figure 2)
- Figure S7 (related to Figure 3)
- Figure S8 (related to Figure 5)

Supplementary Tables

- Table S1
- Table S2
- Table S3
- Table S4

(in Excel-format)

Figure S1

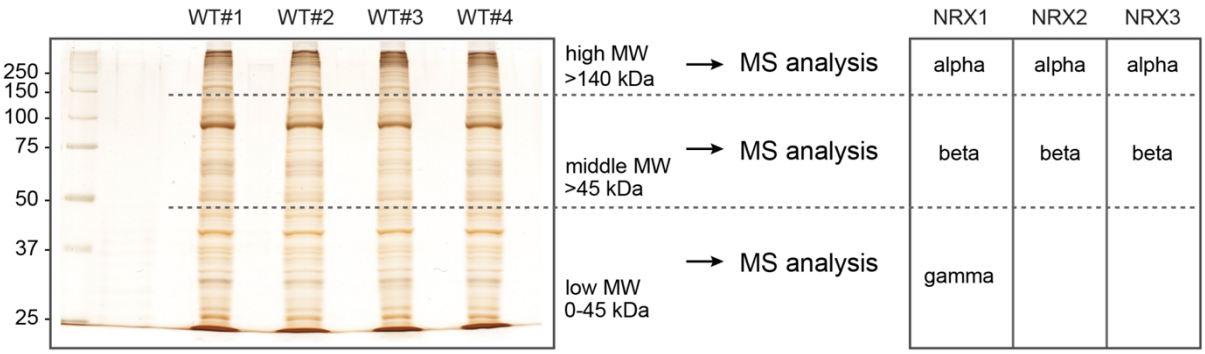

Figure S1
Protein abundances of NRX isoforms
Relative abundance of NRX isoforms (alpha, beta, gamma) was determined by quantitative MS in un-solubilized membrane fractions prepared from adult mouse brains. Proteins were separated by denaturing SDS-PAGE, the gel was cut at 45 and 140 kDa and protein abundance was determined in individual sections. Sequence information unique for NRX1γ were exclusively found in lower molecular weight (MW) sections, peptides unique for NRX1β were identified between 45-140 kDa. All peptides matching the NRX1γ sequence in the 0-45 kDa sections were used to calculate the abundance of this NRX proteoform. Similarly, protein abundances of NRX1β and NRX1α were determined from the middle and high MW sections, respectively.

Figure S2
Coverage of primary sequences of NRX isoforms detected in pan-NRX1-3 APs
Peptides identified by mass spectrometry are in red; those accessible to, but not identified in MS/MS analyses are in black, and peptides hardly or not accessible to our MS/MS analyses (peptide mass >3 kDa or < 738 Da) are given in grey. Absolute coverage is ‘identified sequences / protein sequence’, relative coverage is ‘identified sequences / MS-accessible protein sequence’..

NRX1A_MOUSE - Neurexin-1

Coverage is **71.0%** absolute, **92.4%** relative

```
0001 MGTALVQRGG CCLLCLSLLL LGCWAELGSG LEFPGAEGQW TRFPKWNACC
0051 ESEMSFQLKT RSARGLVLYF DDEGFCDFLE LILTRGGRLQ LSFSIFCAEP
0101 ATLLADTPVN DGAWHSVRIR RQFRNTTLYI DRAEAKWVEV KSKRRDMTVF
0151 SGLFVGGLPP ELRAAALKLT LASVREREPF KGWIRDVRVN SSQALPVDGG
0201 EVKLDDEPPN SGGGSPCEAG EEGEGGVCLN GGVCSVVDDQ AVCDCSRTGF
0251 RGKDCSQEDN NVEGLAHLMM GDQGKSKGKE EYIATFKGSE YFCYDLSQNP
0301 IQSSSDEITL SFKTLQRNGL MLHTGKSADY VNLALKNGAV SLVINLGSGA
0351 FEALVEPVNG KFNDNAWHDV KVTRNLRQHS GIGHAMVNKL HCSVTISVDG
0401 ILTTTGYTQE DYTMLGSDDF FYVGGSPSTA DLPGSPVSNN FMGCLKEVVY
0451 KNNDVRLELS RLAKQGDPKM KIHGVVAFKC ENVATLDPIT FETPESFISL
0501 PKWNAKKTGS ISFDFRTTEP NGLILFSHGK PRHQKDAKHP QMIKVDFFAI
0551 EMLDGHLYLL LDMGSGTIKI KALQKKVNDG EWYHVDFQRD GRSGTISVNT
0601 LRTPYTAPGE SEILDLDDEL YLGGLPENKA GLVFPTEVWT ALLNYGYVGC
0651 IRDLFIDGQS KDIRQMAEIQ STAGVKPSCS KETAKPCLSN PCKNNGMCRD
0701 GWNRYVCDCS GTGYLGRSCE REATVLSYDG SMFMKIQLPV VMHTEAEDVS
0751 LRFRSQRAYG ILMATTSRDS ADTLRLELDA GRVKLTVNLD CIRINCNSSK
0801 GPETLFAGYN LNDNEWHTVR VVRRGKSLKL TVDDQQAMTG QMAGDHTRLE
0851 FHNIETGIIT ERRYLSSVPS NFIGHLQSLT FNGMAYIDLC KNGDIDYCEL
0901 NARFGFRNII ADPVTFKTKS SYVALATLQA YTSMHLFFQF KTTSLDGLIL
0951 YNSGDGNDFI VVELVKGYLH YVFDLGNGAN LIKGSSNKPL NDNQWHNVMI
1001 SRDTSNLHTV KIDTKITTQI TAGARNLDLK SDLYIGGVAK ETYKSLPKLV
1051 HAKEGFQGCL ASVDLNGRLP DLISDALFCN GQIERGCEGP STTCQEDSCS
1101 NQGVCLQQWD GFSCDCSMTS FSGPLCNDPG TTYIFSKGGG QITYKWPPND
1151 RPSTRADRLA IGFSTVQKEA VLVRVDSSSG LGDYLELHIH QGKIGVKFNV
1201 GTDDIAIEES NAIINDGKYH VVRFTRSGGN ATLQVDSWPV IERYPAGNND
1251 NERLAIARQR IPYRLGRVVD EWLLDKGRQL TIFNSQATII IGGKEQGQPF
1301 QGQLSGLYYN GLKVLNMAAE NDANIAIVGN VRLVGEVPSS MTTESTATAM
1351 QSEMSTSIME TTTTLATSTA RRGKPPTKEP ISQTTDDILV ASAECPSDDE
1401 DIDPCEPSSG GLANPTRVGG REPYPGSAEV IRESSSTTGM VVGIVAAAAL
1451 CILILLYAMY KYRNRDEGSY HVDESRNYIS NSAQSNGAVV KEKQPSSAKS
1501 ANKNKKNKDK EYYV
```

NRX1B_MOUSE - Neurexin-1-beta

Coverage is **65.8%** absolute, **89.3%** relative

```
0001 MYQRMLRCGA DLGSPGGGSG GGAGGRLALI WIVPLTLSGL LGVAWGASSL
0051 GAHHIHHFHG SSKHHSVPIA IYRSPASLRG GHAGTTYIFS KGGGQITYKW
0101 PPNDRPSTRA DRLAIGFSTV QKEAVLVRVD SSSGLGDYLE LHIHQGKIGV
0151 KFNVGTDDIA IEESNAIIND GKYHVVRFTR SGGNATLQVD SWPVIERYPA
0201 GNNDNERLAI ARQRIPYRLG RVVDEWLLDK GRQLTIFNSQ ATIIIGGKEQ
0251 GQPFQGQLSG LYYNGLKVLN MAAENDANIA IVGNVRLVGE VPSSMTTEST
0301 ATAMQSEMST SIMETTTTLA TSTARRGKPP TKEPISQTTD DILVASAECP
0351 SDDEDIDPCE PSSGGLANPT RVGGREPYPG SAEVIRESSS TTGMVVGIVA
0401 AAALCILILL YAMYKYRNRD EGSYHVDESR NYISNSAQSN GAVVKEKQPS
0451 SAKSANKNKK NKDKEYYV
```

NRX1G_MOUSE - Neurexin-1-gamma

Coverage is **38.7%** absolute, **80.8%** relative

```
0001 MDMRWHCENS QTTDDILVAS AECPSDDEDI DPCEPSSGGL ANPTRVGGRE
0051 PYPGSAEVIR ESSSTTGMVV GIVAAAALCI LILLYAMYKY RNRDEGSYHV
0101 DESRNYISNS AQSNGAVVKE KQPSSAKSAN KNKKNKDKEY YV
```

NRX2A_MOUSE - Neurexin-2

Coverage is **62.2%** absolute, **84.4%** relative

```
0001 MALGSRWQPP PQLPPLLLLL ALAAGVRGLE FGGGPGQWAR YARWAGAAST
0051 GELSFSLRTN ATRALLLYLD DGGDCDFLEL LLVDGRLRLR FTLSCAEPAT
0101 LQLDTPVADD RWHMVLLTRD ARRTALAVDG EARAAEVRSK RREMQVASDL
0151 FVGGIPPDVR LSALTLSTVK YEPPFRGLLA NLKLGERPPA LLGSQGLRGA
0201 AADPLCAPAR NPCANGGLCT VLAPGEVGCD CSHTGFGGKF CSEEEHPMEG
0251 PAHLTLNSEV GSLLFSEGGA GRGGAGDVHQ PTKGKEEFVA TFKGNEFFCY
0301 DLSHNPIQSS TDEITLAFRT LQRNGLMLHT GKSADYVNLS LKSGAVWLVI
0351 NLGSGAFEAL VEPVNGKFND NAWHDVRVTR NLRQHAGIGH AMVNKLHYLV
0401 TISVDGILTT TGYTQEDYTM LGSDDFFYIG GSPNTADLPG SPVSNNFMGC
0451 LKDVVYKNND FKLELSRLAK EGDPKMKLQG DLSFRCEDVA ALDPVTFESP
0501 EAFVALPRWS AKRTGSISLD FRTTEPNGLL LFSQGRRAGA GVGSHSSTQR
0551 ADYFAMELLD GYLYLLLDMG SGGIKLRASS RKVNDGEWCH VDFQRDGRKG
0601 SISVNSRSTP FLATGESEVL DLESELYLGG LPEGGRVDLP LPPEVWTAAL
0651 RAGYVGCVRD LFIDGRSRDL RGLAEAQGAV GVAPFCSRET LKQCASAPCR
0701 NGGICREGWN RFVCDCIGTG FLGRVCEREA TVLSYDGSMY MKIMLPTAMH
0751 TEAEDVSLRF MSQRAYGLMM ATTSRESADT LRLELDGGQM RLTVNLDCLR
0801 VGCAPSKGPE TLFAGHKLND NEWHTVRVVR RGKSLQLSVD NVTVEGQMAG
0851 AHTRLEFHNI ETGIMTERRF ISVVPSNFIG HLSGLVFNGQ PYMDQCKDGD
0901 ITYCELNARF GLRAIVADPV TFKSRSSYLA LATLQAYASM HLFFQFKTTA
0951 PDGLLLFNSG NGNDFIVIEL VKGYIHYVFD LGNGPSLMKG NSDKPVNDNQ
1001 WHNVVVSRDP GNVHTLKIDS RTVTQHSNGA RNLDLKGELY IGGLSKNMFS
1051 NLPKLVASRD GFQGCLASVD LNGRLPDLIA DALHRIGQVE RGCDGPSTTC
1101 TEESCANQGV CLQQWDGFTC DCTMTSYGGP VCNDPGTTYI FGKGGALITY
1151 TWPPNDRPST RMDRLAVGFS THQRSAVLVR VDSASGLGDY LQLHIDQGTV
1201 GVIFNVGTDD ITIDEPNAIV SDGKYHVVRF TRSGGNATLQ VDSWPVNERY
1251 PAGNFDNERL AIARQRIPYR LGRVVDEWLL DKGRQLTIFN SQAAIKIGGR
1301 DQGRPFQGQV SGLYYNGLKV LALAAESDPN VRTEGHLRLV GEGPSVLLSA
1351 ETTATTLLAD MATTIMETTT TMATTTTRRG RSPTMRDSTT QNTDDLLVAS
1401 AECPSDDEDL EECEPSTGGE LILPIITEDS LDPPPVATRS PFVPPPPTFY
1451 PFLTGVGATQ DTLPPPAARR PSSGGPCQAE RDDSDCEEPV EASGFASGEV
1501 FDSSLPPTDD EDFYTTFPLV TDRTTLLSPR KPRPNLRTDG ATGAPGVLFA
1551 PSAPAPNLPA GKMNHRDPLQ PLLENPPLGP GVPTAFEPRR PPPLRPGVTS
1601 APGFPRLPTA NPTGPGERGP PGAVEVIRES SSTTGMVVGI VAAAALCILI
1651 LLYAMYKYRN RDEGSYQVDQ SRNYISNSAQ SNGAVVKEKA PAAPKTPSKA
1701 KKNKDKEYYV
```

NRX2B_MOUSE - Neurexin-2-beta

Coverage is **43.9%** absolute, **78.8%** relative.

```
0001 MPPGGSGQGG CPRRPPALAG PLPPPPPPPP LPLLLGLLLL LGAAEGARVS
0051 SSLSTTHHVH HFHSKHGTVP IAINRMPFLT RSGHAGTTYI FGKGGALITY
0101 TWPPNDRPST RMDRLAVGFS THQRSAVLVR VDSASGLGDY LQLHIDQGTV
0151 GVIFNVGTDD ITIDEPNAIV SDGKYHVVRF TRSGGNATLQ VDSWPVNERY
0201 PAGNFDNERL AIARQRIPYR LGRVVDEWLL DKGRQLTIFN SQAAIKIGGR
0251 DQGRPFQGQV SGLYYNGLKV LALAAESDPN VRTEGHLRLV GEGPSVLLSA
0301 ETTATTLLAD MATTIMETTT TMATTTTRRG RSPTLMDSTT QNTDDLLVAS
0351 AECPSDDEDL EECEPSTGGE LILPIITEDS LDPPPVATRS PFVPPPPTFY
0401 PFLTGVGATQ DTLPPPAARR PSSGGPCQAE RDDSDCEEPV EASGFASGEV
0451 FDSSLPPTDD EDFYTTFPLV TDRTTLLSPR KPRPNLRTDG ATGAPGVLFA
0501 PSAPAPNLPA GKMNHRDPLQ PLLENPPLGP GVPTAFEPRR PPPLRPGVTS
0551 APGFPRLPTA NPTGPGERGP PGAVEVIRES SSTTGMVVGI VAAAALCILI
0601 LLYAMYKYRN RDEGSYQVDQ SRNYISNSAQ SNGAVVKEKA PAAPKTPSKA
0651 KKNKDK EYYV
```

NRX3A_MOUSE - Neurexin-3

Coverage is **57.1%** absolute, **75.3%** relative

```
0001 MSFTLHSVFF TLKVSIFLGS LVGLCLGLEF MGLPNQWARY LRWDASTRSD
0051 LSFQFKTNVS TGLLLYLDDG GVCDFLCLSL VDGRVQLRFS MDCAETTVLS
0101 NKQVNDSSWH FLMVSRDRVR TGLVIDGEGQ SGELRPQRPY MDVVSDLFLG
0151 GVPADIRPSA LTLDGVQSMP GFKGLMLDLK YGNSEPRLLG SQSVQLEAEG
0201 PCGERPCENG GICFLLDGHP TCDCSTTGYG GTLCSEDVSQ GPGLSHLMMS
0251 EQAREENVAT FRGSEYLCYD LSQNPIQSSS DEITLSFKTW QRNGLILHTG
0301 KSADYVNLAL KDGAVSLVIN LGSGAFEAIV EPVNGKFNDN AWHDVKVTRN
0351 LRQVTISVDG ILTTTGYTQE DYTMLGSDDF FYVGGSPSTA DLPGSPVSNN
0401 FMGCLKEVVY KNNDIRLELS RLARIGDTKM KIYGEVVFKC ENVATLDPIN
0451 FETPEAYISL PKWNTKRMGS ISFDFRTTEP NGLILFTHGK PQERKDVRSQ
0501 KNTKVDFFAV ELLDGNLYLL LDMGSGTIKV KATQKKANDG EWYHVDIQRD
0551 GRSGTISVNS RRTPFTASGE SEILDLEGDM YLGGLPENRA GLILPTELWT
0601 AMLNYGYVGC IRDLFIDGRS KNIRQLAEMQ NAAGVKSSCS RMSAKQCDSY
0651 PCKNNAVCKD GWNRFICDCT GTGYWGRTCE REASILSYDG SMYMKVIMPM
0701 VMHTEAEDVS FRFMSQRAYG LLVATTSRDS ADTLRLELDG GRVKLMVNLD
0751 CIRINCNSSK GPETLYAGQK LNDNEWHTVR VVRRGKSLKL TVDDDVAEGT
0801 MVGDHTRLEF HNIETGIMTE KRYISVVPSS FIGHLQSLMF NGLLYIDLCK
0851 NGDIDYCELK ARFGLRNIIA DPVTFKTKSS YLTLATLQAY TSMHLFFQFK
0901 TTSADGFILF NSGDGNDFIA VELVKGYIHY VFDLGNGPNV IKGNSDRPLN
0951 DNQWHNVVIT RDSSNTHSLK VDTKVVTQVI NGAKNLDLKG DLYMAGLAQG
1001 MYSNLPKLVA SRDGFQGCLA SVDLNGRLPD LINDALHRSG QIERGCEGPS
1051 TTCQEDSCAN QGVCMQQWEG FTCDCSMTSY SGNQCNDPGA TYIFGKSGGL
1101 ILYTWPANDR PSTRSDRLAV GFSTTVKDGI LVRIDSAPGL GDFLQLHIEQ
1151 GKIGVVFNIG TVDISIKEER TPVNDGKYHV VRFTRNGGNA TLQVDNWPVN
1201 EHYPTGNTDN ERLQMVKQKI PFKYNRPVEE WLQEKGRQLT IFNTQAQIAI
1251 GGKDKGRLFQ GQLSGLYYDG LKVLNMAAEN NPNIKINGSV RLVGEVPSVS
1301 GTTQTTSMPP EMSTTVMETT TTMATTTTRK NRSTASIQPT SDDLVSSAEC
1351 SSDDEDFVEC EPSTDKSLST SIFEGGYKAH APKWESKDFR PNKVSETSRT
1401 TTTSLSPELI RFTASSSSGM VPKLPAGKMN NRDLKPQPDI VLLPLPTAYE
1451 LDSTKLKSPL ITSPMFRNVP TANPTEPGIR RVPGASEVIR ESSSTTGMVV
```

```
1501 GIVAAAALCI LILLYAMYKY RNRDEGSYQV DETRNYISNS AQSNGTLMKE
1551 KQASSKSGHK KQKNKDKEYY V
```

NRX3B_MOUSE - Neurexin-3-beta

Coverage is **56.1%** absolute, **78.7%** relative

```
0001 MHLRIHPRRS PPRRPAWTLG IWSLFWGCIV SSVWSSSNVA SSSSSSPGSH
0051 SQQEHHFHGS KHHSVPISIY RSPVSLRGGH AGATYIFGKS GGLILYTWPA
0101 NDRPSTRSDR LAVGFSTTVK DGILVRIDSA PGLGDFLQLH IEQGKIGVVF
0151 NIGTVDISIK EERTPVNDGK YHVVRFTRNG GNATLQVDNW PVNEHYPTGN
0201 TDNERLQMVK QKIPFKYNRP VEEWLQEKGR QLTIFNTQAQ IAIGGKDKGR
0251 LFQGQLSGLY YDGLKVLNMA AENNPNIKIN GSVRLVGEVP SVSGTTQTTS
0301 MPPEMSTTVM ETTTTMATTT TRKNRSTASI QPTSDDLVSS AECSSDDEDF
0351 VECEPSTGRS DKSLSTSIFE GGYKAHAPKW ESKDFRPNKV SETSRTTTTS
0401 LSPELIRFTA SSSSGMVPKL PAGKMNNRDL KPQPDIVLLP LPTAYELDST
0451 KLKSPLITSP MFRNVPTANP TEPGIRRVPG ASEVIRESSS TTGMVVGIVA
0501 AAALCILILL YAMYKYRNRD EGSYQVDETR NYISNSAQSN GTLMKEKQAS
0551 SKSGHKKQKN KDKEYYV
```

Figure S3

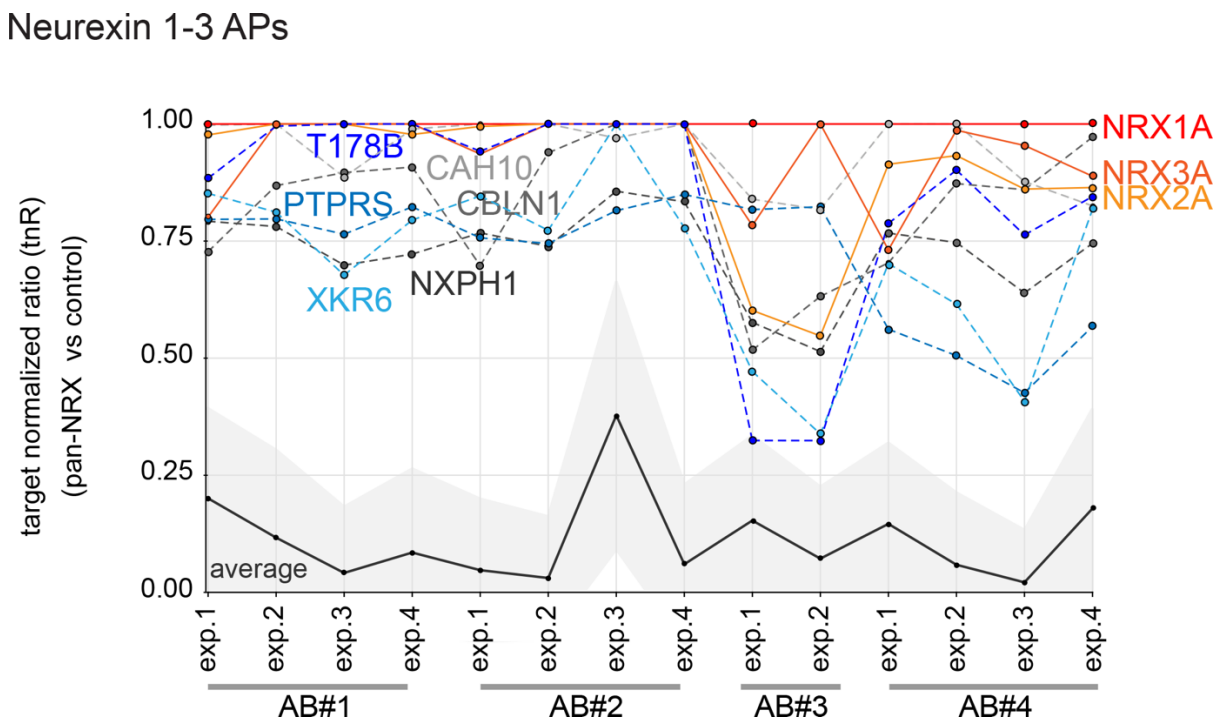

Figure S3

tnR profiles of anti-Nrx1-3 APs

Target-normalized ratio (tnR)-values of selected proteins specifically (co-)purified in 12 anti-NRX1-3 APs with four different anti-NRX1-3 ABs (see also Figure 1C). tnR-values >0.25 indicate specific co-purification (with the target). Average indicates average-tnRs calculated from all MS-identified proteins in the respective AP-eluate, grey area represents SDs of these average-tnRs.

Figure S4

Expression pattern of NRX1-3, T178A/B and PTPRD/S/F in mouse brain

Transcriptome data were extracted from the DropViz data base (Saunders et al., 2018)). Number of RNA transcripts per 100,000 unique molecular identifiers in the indicated brain regions and meta-groups according to DropViz single-cell transcriptomics data. CA1: CA1 pyramidal cells, CA3: CA3 pyramidal cells, DG: dentate gyrus, MC: mossy cells, IN: interneurons, GC: granule cells, PC: pyramidal cells, DRD1/2: dopamine receptor D1/2, GAD: glutamic acid decarboxylase.

Note ubiquitous expression all of core-module constituents in both neurons and glia and distinct patterns for T178A (predominantly found in cerebellum).

Figure S4

Expression pattern of Nrx-T178-rPTP module components

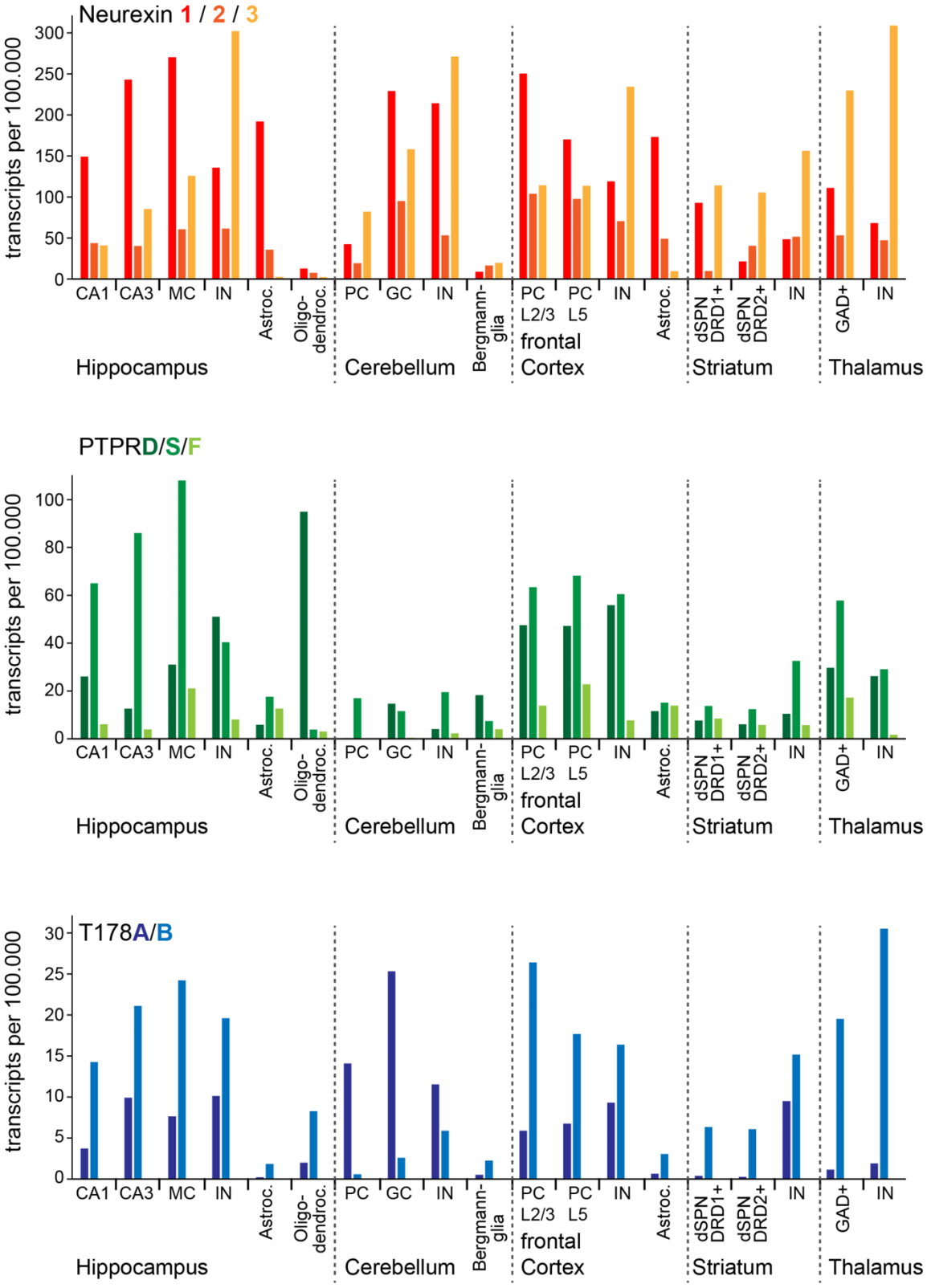

Figure S5

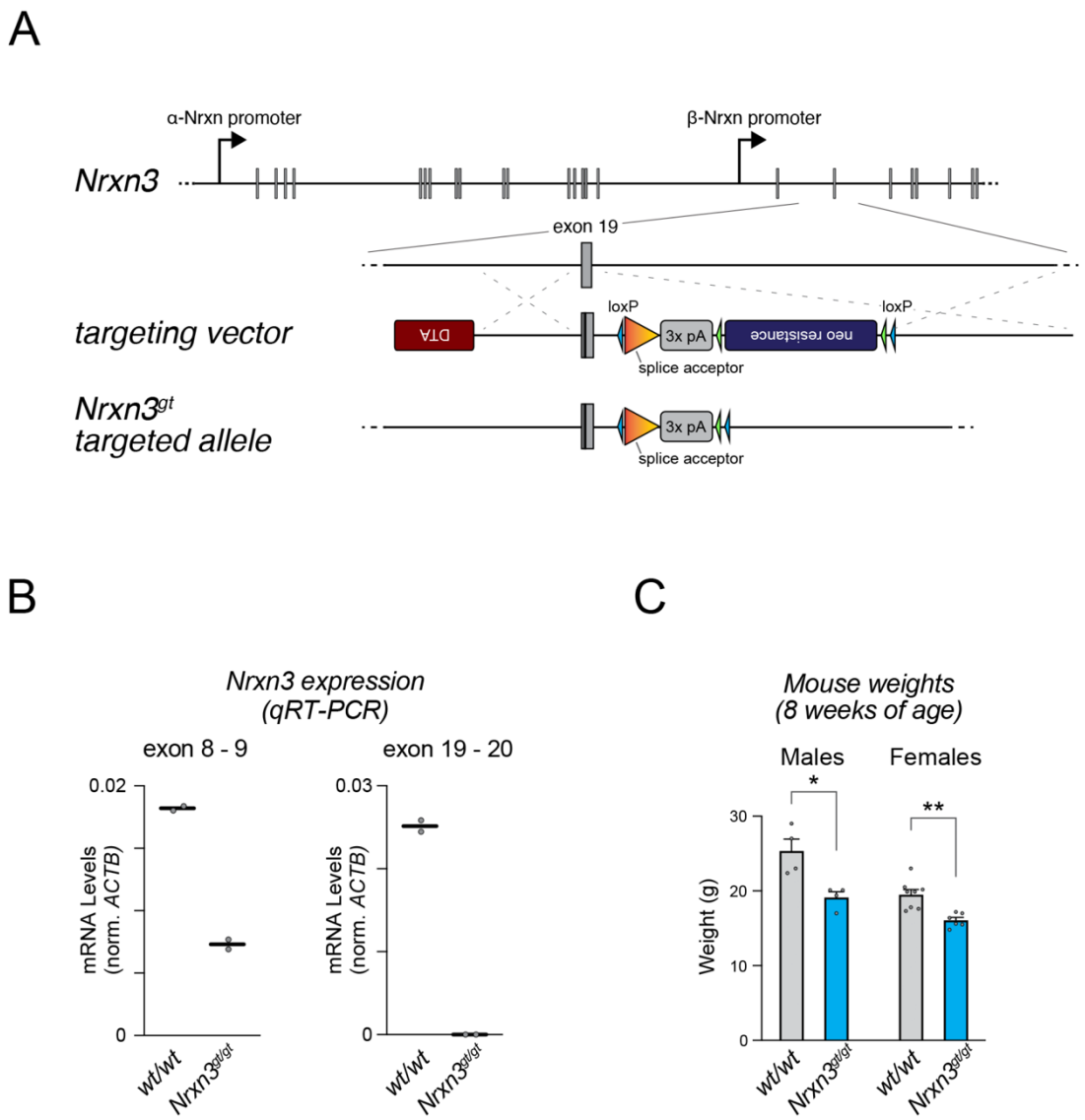

Figure S5

Design and validation of NRX3 KO mice.

(**A**) Design of the targeting vector for gene-trap mutagenesis of NRX3 in mice. The gene-trap construct was introduced after the first exon common to both α- and β-isoforms. (**B**) Gene-trap insertion result in loss of mRNA. Levels of Nrxn3 transcripts before and after the targeted intron, respectively, monitored by qRT-PCR. (**C**) Mouse weight at 8 weeks of age. *, $p < 0.05$ and **, $p < 0.01$ by two-tailed students t-test.

Figure S6

A

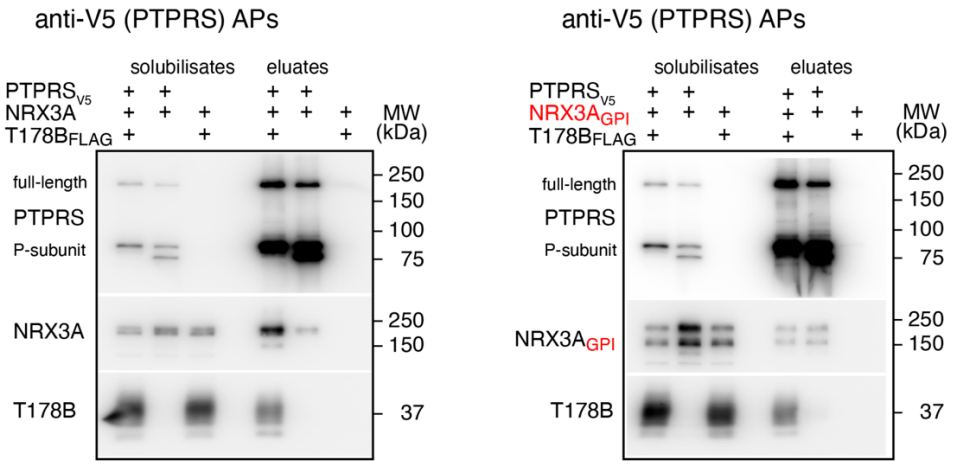

B

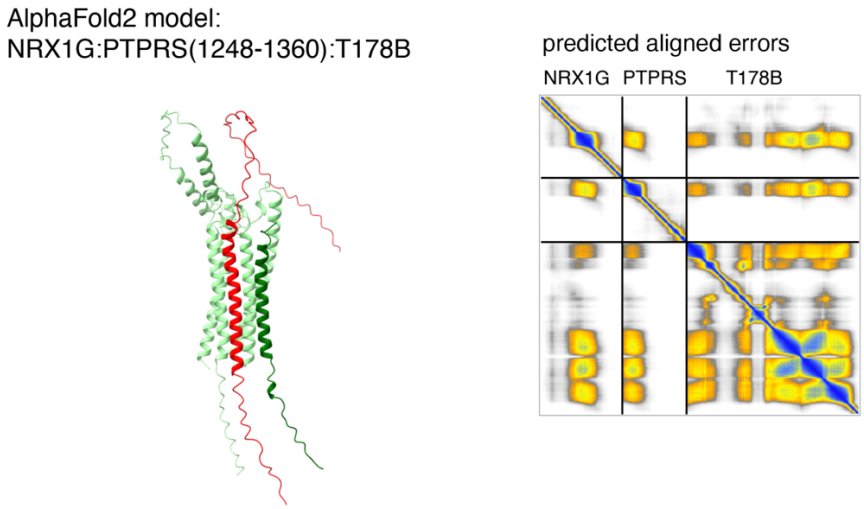

Figure S6

(**A**) **Reconstitution of NRX3A, T178B and PTPRS complexes**

Western-probed SDS-PAGE separations of input and eluates of APs with anti-V5 ABs from tsA201 cells transiently expressing V5-tagged PTPRs, FLAG-tagged T178B and either NRX3A or a splice variant of NRX3A lacking the transmembrane domain and attached to the membrane via a GPI-anchor. Note that the presence of T178B appears critical for stable complex formation with NRX3A (similar as NRX1A, Figure 2E). In contrast, binding of NRX3A-GPI to PTPRS is weak and independent of the presence of T178B.

(**B**) **Details to structural predictions by AlphaFold**

Prediction of 3D-structural arrangement of the membrane-close region of the core-module composed of NRX1γ (mouse, aa 1-139, full length), PTPRS (mouse, aa 1251-1360) and T178B (human, 1-294, full length) by AlphaFold2-Multimer. Predicted

aligned errors (PAE) provide estimates for the confidence of the correct position of two residues in the structure. Note high-confidence levels (colored blue) were only observed in the transmembrane regions; lower confidence levels are shown in yellow.

Figure S7

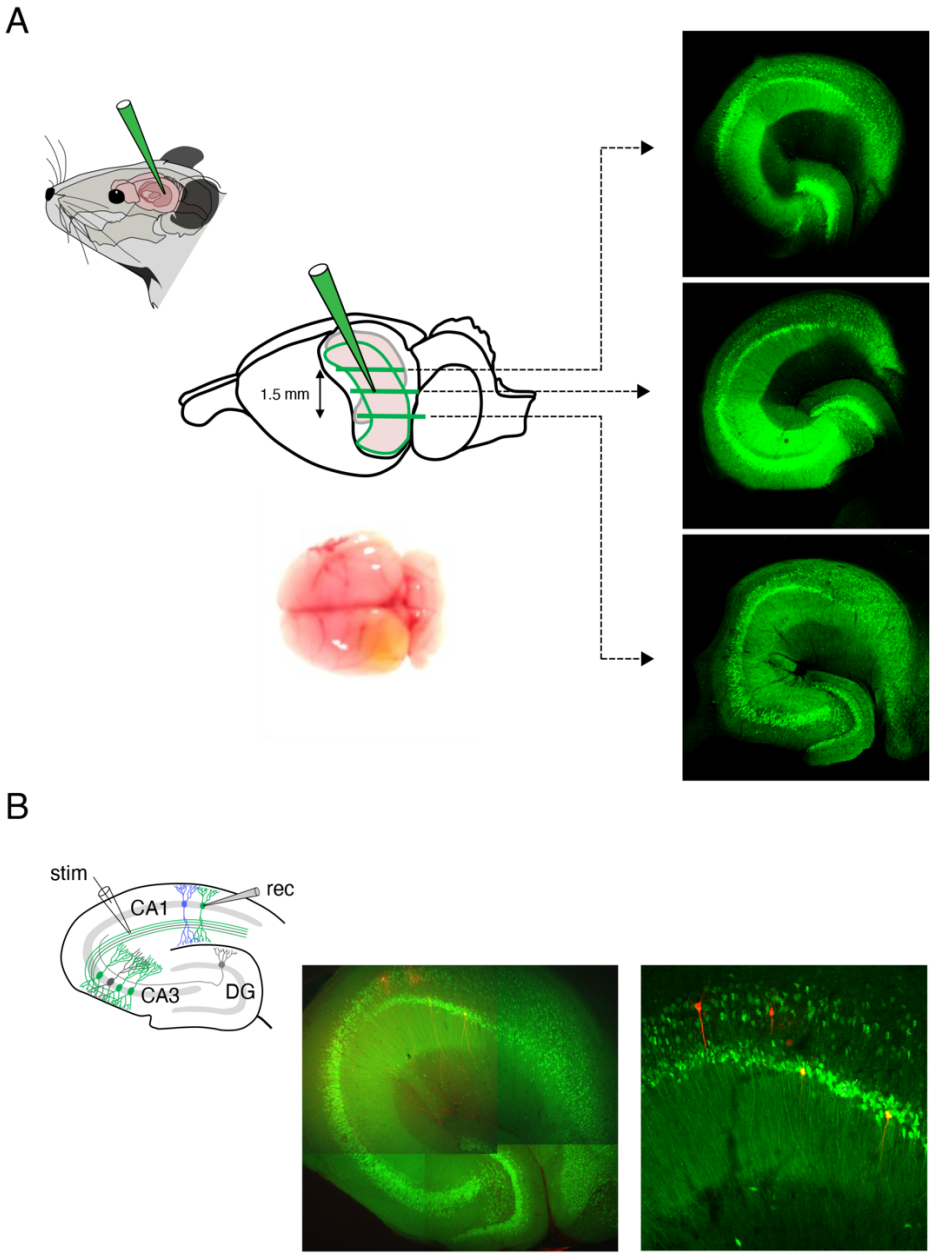

Figure S7

Stereotactic injections of AAV expressing sh-T178B into hippocampal CA3 regions and somatic recordings in CA1 pyramidal cells of adult mice

(**A**), Scheme depicting stereotactic injection into the hippocampal CA3 region and confocal images showing GFP-fluorescence in three brain slices to document spreading and transfection of cells by the AAV particles; GFP-expression is driven by

the ubiquitin promotor (see generation of AAV-virus in STAR Methods). Inset: Image showing unilateral injection into the left hemisphere.
(**B**) Scheme illustrating slice-recordings of CA1 PCs in whole cell configuration and confocal images indicating four CA1 PCs filled with biocytin (red fluorescence) through the patch-pipette during recordings. Note two of these cells were infected by the AAV (yellow fluorescence), two cells were non-infected (red fluorescence).

Figure S8

Organisation of protein networks

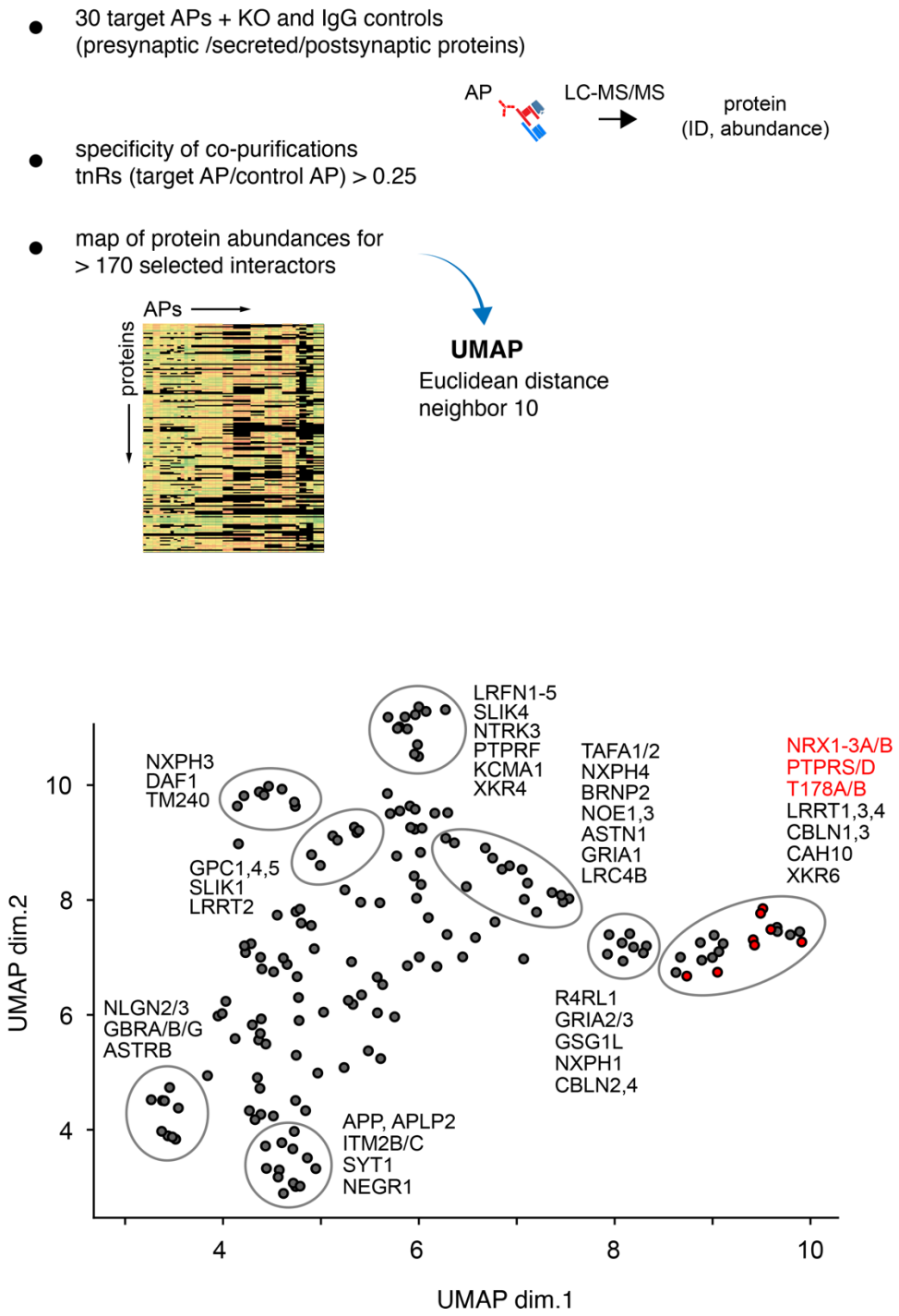

Figure S8

UMAP (Uniform Manifold Approximation and Projection, (Sainburg et al., 2021)) cluster-analysis performed with the MS-derived abundance values of all proteins (total of 172) that were specifically co-purified in NRX1-3 and reverse APs with a total of 30 different target proteins. UMAP-derived subclusters (of similar behavior over the entire set of APs) were encircled with selected constituents annotated.

Supplementary Tables

Table S1

tnR-values of APs with the anti-NRX1-3 ABs (Table 1), and with the sub-type specific anti-NRX1, 2, 3 ABs

Table S2

tnR-values of APs with anti-NRX1-3 and anti-PTPRs ABs from ER-membranes

Table S3

Protein abundance ratios determined in membrane fractions from cortical cultures infected with AAV: sh-T178B or control AAV: GFP.

Table S4

tnR-values of specifically co-purified proteins in target APs indicated in Figure 5